PHYSICAL REVIEW B **66**, 024515 (2002)

Vortex structure of thin mesoscopic disks in the presence of an inhomogeneous magnetic field

M. V. Milošević, S. V. Yampolskii,* and F. M. Peeters†
Departement Natuurkunde, Universiteit Antwerpen (UIA), Universiteitsplein 1, B-2610 Antwerpen, Belgium

(Received 18 July 2001; revised manuscript received 5 October 2001; published 17 July 2002)

The vortex states in a thin mesoscopic disk are investigated within the phenomenological Ginzburg-Landau theory in the presence of different ‘‘model’’ magnetic-field profiles with zero average field, which may result from a ferromagnetic disk or circulating currents in a loop near the superconductor. We calculated the dependences of both the ground and metastable states on the magnitude and shape of the magnetic-field profile for different values of the order-parameter angular moment, i.e., the vorticity. The regions of existence of the multivortex state and the giant-vortex state are found. We analyzed the phase transitions between these states and studied the contribution from ring-shaped vortices. An additional transition between different multivortex configurations and the ground state is found. Furthermore, we found a vortex state consisting of a central giant vortex surrounded by a collection of antivortices which are located in a ring around this giant vortex. The limit to a disk with an infinite radius, i.e., a film, will also be discussed. We also extended our results to ‘‘real’’ magnetic-field profiles and to the case in which an external homogeneous magnetic field is present.

DOI: 10.1103/PhysRevB.66.024515 PACS number(s): 74.60.Ec, 74.60.Ge, 74.80.−g, 74.25.Dw

I. INTRODUCTION

Recent progress in microfabrication and measurement techniques makes it possible to study the properties of small superconducting structures, so-called mesoscopic samples, with sizes comparable to the penetration depth λ and the coherence length ξ. Mesoscopic disks have been one of the most popular and exciting study objects[1–13] in this respect. The behavior of such mesoscopic samples in an external magnetic field is strongly influenced by the boundary conditions, sample size, and geometry and may lead to various superconducting states and phase transitions between them.

Motivated by recent experiments,[14,15] we study the properties of a superconducting disk in the presence of a steplike external magnetic field. The steplike field profile is a model magnetic-field profile for a ferromagnetic dot or current loop placed on top of the superconductor. These profiles have the important property that the average magnetic field is zero. We investigate the influence of step height, step profile, and the ratio between step width and radius of the disk on the superconducting phase diagram.

Previous investigations of structures with magnetic dots were limited to experiments with superconducting films deposited on regular arrays of magnetic dots[14–16] and theoretical studies of single magnetic dots embedded in a thin superconducting film.[17,18] The common problem was that, for magnetic dots, the strong field present inside the ferromagnet suppresses the superconducting order parameter, and in such situations it is appropriate to adopt a boundary condition in which the order parameter itself vanishes. This seems to spoil the effect that leads to surface superconductivity, and it is not at first obvious why magnetic dots should support the relatively large supercurrents associated with multiple vortices. Although enhancement of superconducting order is preserved in the vicinity of the dot due to the fringing field of the dot itself,[18] a possible oxide layer between the magnetic dot and the superconductor may restore the boundary condition to that of a superconductor/insulator interface and make this effect more distinctive. In the present paper we put a single magnetic dot on top of the superconductor and study the behavior of our sample in such a nonuniform magnetic field of the dot, which enhances the possibility of obtaining various combinations of superconducting states. To better understand the problem we start from a simple theoretical model for the inhomogeneous magnetic-field profile that, we believe, captures all aspects of the physics involved. Models used before vary from a representation of the magnetic dot by a perfect dipole[19] to a magnetic-field profile calculated numerically for an infinitely thin magnetic disk.[17] To obtain a better insight we start first with a simple steplike field model and subsequently investigate the more complicated real magnetic-field profiles, which we obtained numerically.

Theoretical studies have predicted that in mesoscopic disks surrounded by an insulating media, three kinds of superconducting states can exist—giant-vortex state (a circular symmetric state with a fixed value of angular momentum), multivortex state (a collection of single vortices which can be obtained as a linear combination of giant vortices with different angular momenta), and ring-shaped vortex states[20,21] with larger energy than giant-vortex and multivortex states. The ring-shaped two-dimensional vortex states have a cylindrically symmetric magnetic-field profile and they are different from the ring vortices which are, e.g., found in three-dimensional superfluid liquid helium. In the present paper we observe giant vortex states and first-order transitions between them,[4,6] and for sufficiently large disks, multivortex structures, which are the analog of the Abrikosov flux-line lattice in a bulk superconductor. The latter results not only from a mixture of giant-vortex states but also from giant-ring vortex combinations as well. The latter one may even lead to an off-center location of a single vortex or multivortices. Moreover, with changing strength of the field there is a transition between giant-giant and giant-ring multivortex states. Increasing the step height of the magnetic-field profile we found reentrant behavior, i.e., a transition from the giant-vortex to the multivortex state and back to the giant-vortex state before superconductivity is destroyed.[7] We found that for sufficiently large magnetic disks vortex/

antivortex structures can be formed (giant-multiantivortex state). In order to investigate these different vortex structures we use the method proposed by Schweigert *et al.*[7] and Palacios,[8,9] with its semianalytical extensions of Ref. 20 to determine the stability of the different multivortex configurations. In particular, the analysis of Ref. 20 showed that in a superconducting disk the ring-shaped vortices are unstable in the presence of a homogeneous magnetic field.

Our analysis is within the framework of the phenomenological Ginzburg-Landau (GL) theory. Although this theory has a firm mathematical derivation only in a narrow range of magnetic field close to the superconducting-normal state boundary, it has been found that it gives also very good results deep inside the superconducting phase diagram.[4,6]

The paper is organized as follows. In Sec. II we present our theoretical model. In Sec. III we discuss the giant-vortex states and study the influence of a step magnetic-field profile, with zero average, which is centered at the disk or has a ring symmetry, on the superconducting state. These step profiles are limiting cases of the actual experimentally realizable profiles. The stability of multivortex states and transitions between them are investigated in Sec. IV. The interest in this study is shown through different H_{in}-R phase diagrams in Sec. V, where H_{in} is the magnitude of the magnetic-field profile and R represents the radius (of the superconducting disk, magnetic dot, current loop, etc.). In Sec. VI we present the results of our approach applied to a superconducting disk in the presence of an experimentally realizable real magnetic dot and current loop field profile. Section VII is an extension of previous sections where the influence of an additional homogeneous background magnetic field is investigated. Our conclusions are given in Sec. VIII.

II. THEORETICAL MODEL

We consider a mesoscopic superconducting disk with radius R and thickness d surrounded by vacuum. The external magnetic field $\vec{H}=(0,0,H)$ is directed normal to the disk plane. In this paper we investigate two different magnetic-field profiles: (1) steplike magnetic field in the center of the disk, and (2) a ring steplike magnetic-field profile with inner radius of the ring, R_d. The magnetic-field strengths of the profile (Fig. 1) are chosen such that the total magnetic flux equals zero. These models should correspond to the magnetic field of a perpendicular magnetized magnetic dot placed in the center of the disk on top of the superconductor, and the magnetic field due to a current loop placed on the superconductor, respectively. We assume that the superconductor will not alter the magnetic state of the ferromagnetic disk. We have to solve the system of two coupled nonlinear GL equations, which determine the distribution of both the superconducting order parameter, $\Psi(\vec{r})$, and the magnetic field [or vector potential $\vec{A}(\vec{r})$] inside and outside the superconductor

$$\frac{1}{2m}\left(-i\hbar\vec{\nabla}-\frac{2e}{c}\vec{A}\right)^2\Psi=-\alpha\Psi-\beta\Psi|\Psi|^2, \tag{1}$$

$$\vec{\nabla}\times\vec{\nabla}\times\vec{A}=\frac{4\pi}{c}\vec{j}, \tag{2}$$

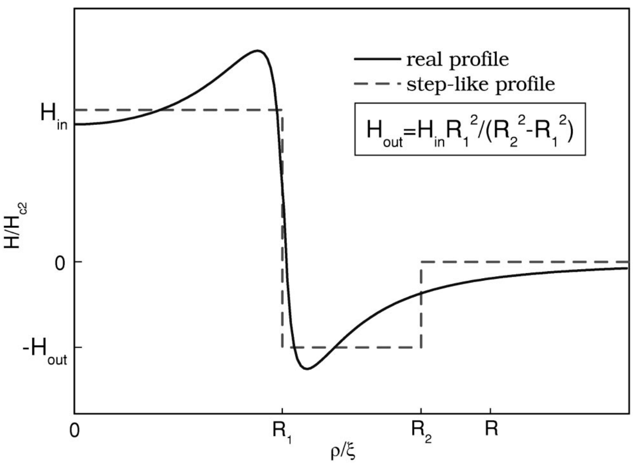

FIG. 1. The magnetic-field profile of the magnetic disk (solid curve) and the corresponding model step profile (dashed curve).

where the density of the superconducting current $\vec{j}$ is given by

$$\vec{j}=\frac{e\hbar}{im}(\Psi^*\vec{\nabla}\Psi-\Psi\vec{\nabla}\Psi^*)-\frac{4e^2}{mc}|\Psi|^2\vec{A}. \tag{3}$$

Here $\vec{r}=(\vec{\rho},z)$ is the three-dimensional position in space. Due to the circular symmetry of the disk we use cylindrical coordinates: ρ is the radial distance from the disk center, φ is the azimuthal angle, and the z axis is taken perpendicular to the disk plane, where the disk lies between $z=-d/2$ and $z=d/2$.

Equations (1)–(3) have to be supplemented by boundary conditions (BC) for $\Psi(\vec{r})$ and $\vec{A}(\vec{r})$:

$$\left(-i\hbar\vec{\nabla}-\frac{2e}{c}\vec{A}\right)\Psi\Big|_n=0, \tag{4}$$

where the subscript n denotes the component normal to the disk surface. The boundary conditions for the vector potential have to be taken far away from the disk where the magnetic field becomes equal to the external field H,

$$\vec{A}|_{r\to\infty}=0. \tag{5}$$

Using dimensionless variables and the London gauge div $\vec{A}=0$ we can rewrite the system of equations (1)–(3) and BC (4) in the following form:

$$(-i\vec{\nabla}-\vec{A})^2\psi=\psi-\psi|\psi|^2, \tag{6}$$

$$-\kappa^2\nabla^2\vec{A}=\frac{1}{2i}(\psi^*\vec{\nabla}\psi-\psi\vec{\nabla}\psi^*)-|\psi|^2\vec{A}, \tag{7}$$

$$(-i\vec{\nabla}-\vec{A})\psi|_n=0. \tag{8}$$

Here all distances are measured in units of the coherence length $\xi=\hbar/\sqrt{2m|\alpha|}$, the order parameter in $\Psi_0=\sqrt{|\alpha|/\beta}$, the vector potential in units of $c\hbar/2e\xi$, $\kappa=\lambda/\xi$ is the GL parameter, and $\lambda=c\sqrt{m/\pi}/4e\Psi_0$ is the London penetration depth. We measure the magnetic field in $H_{c2}=c\hbar/2e\xi^2=\kappa\sqrt{2}H_c$, where $H_c=\sqrt{4\pi\alpha^2/\beta}$ is the thermodynamical critical field.

The free energy of the superconducting state, measured in $F_0=H_c^2V/8\pi$ units, is determined by the expression

$$F=\frac{2}{V}\left\{\int dV[-|\psi|^2+\tfrac{1}{2}|\psi|^4+|-i\vec{\nabla}\psi-\vec{A}\psi|^2+\kappa^2[\vec{h}(\vec{r})-\vec{H}_0]^2]\right\},\tag{9}$$

with the local magnetic field

$$\vec{h}(\vec{r})=\vec{\nabla}\times\vec{A}(\vec{r}).$$

We restrict ourselves to sufficiently thin disks such that $d\ll\xi,\lambda$. In this case, to a first approximation, the magnetic field due to the circulating superconducting currents may be neglected and the total magnetic field equals the external one $\vec{H}_0$. Within this approximation we have to solve only the first GL equation (6) with $\vec{A}=\vec{A}_0$, where $\vec{H}_0=\vec{\nabla}\times\vec{A}_0$. One should notice that in this approach, for different cases, we change only the vector potential profile $\vec{A}_0$. For our step profile

$$H_0(\rho)=\begin{cases}0, & 0\leqslant\rho\leqslant R_d\\ H_{in}, & R_d\leqslant\rho\leqslant R_1\\ -H_{out}, & R_1\leqslant\rho\leqslant R_2\\ 0, & R_2\leqslant\rho\leqslant R,\end{cases}\tag{10}$$

the vector potential is given by

$$A_0(\rho)=\begin{cases}0, & 0\leqslant\rho\leqslant R_d\\ \dfrac{H_{in}}{2}\left(\rho-\dfrac{R_d^2}{\rho}\right), & R_d\leqslant\rho\leqslant R_1\\ \dfrac{H_{in}}{2\rho}(R_1^2-R_d^2)-\dfrac{H_{out}}{2}\left(\rho-\dfrac{R_1^2}{\rho}\right), & R_1\leqslant\rho\leqslant R_2\\ 0, & R_2\leqslant\rho\leqslant R,\end{cases}\tag{11}$$

where H_{in} describes the positive step and $H_{out}=H_{in}(R_1^2-R_d^2)/(R_2^2-R_1^2)$ determines the value of the negative step (see Figs. 1 and 20 and the Appendix).

First, we determine the z dependence of $\psi(\vec{r})$. Representing the order parameter as a series over cosines $\psi(\vec{r})=\Sigma_{k=0}^{\infty}\psi_k(\vec{\rho})\cos(k\pi z/d)$ and using the same BC (8) at the disk sides ($z=\pm d/2$) and using the first GL equation (1), one can verify that the uniform part of the order parameter, i.e., the $k=0$ term, gives the main contribution for $(\pi\xi/d)^2\gg1$. Therefore, we may assume that the order parameter is uniform along the z direction of the disk and average the first GL equation over the disk thickness. After this averaging and for a fixed value of the angular momentum, it leads to $\psi(\vec{\rho})=f(\rho)\exp(iL\varphi)$, and the problem for $f(\rho)$ is reduced to a one dimensional problem, as in Ref. 6:

$$-\frac{1}{\rho}\frac{\partial}{\partial\rho}\rho\frac{\partial f}{\partial\rho}+\left\langle\left(\frac{L}{\rho}-A\right)^2\right\rangle f=f(1-f^2),\tag{12}$$

and for the vector potential

$$-\kappa^2\left(\frac{\partial}{\partial\rho}\frac{1}{\rho}\frac{\partial\rho A}{\partial\rho}+\frac{\partial^2 A}{\partial z^2}\right)=\left(\frac{L}{\rho}-A\right)f^2\theta(\rho/R)\theta(2|z|/d),\tag{13}$$

where the function $\theta(x)=1\ (x<1),\ 0\ (x>1)$, and R and d are the dimensionless disk radius and thickness, respectively. The brackets $\langle\cdots\rangle$ refer to averaging over the disk thickness.

III. GIANT-VORTEX STATES

The giant-vortex state has cylindrical symmetry and consequently the order parameter can be written as $\psi(\vec{\rho})=f(\rho)\exp(iL\varphi)$. The stable states are obtained in the following way. From the *linearized* GL equation we find $f(\rho)$ up to a multiplying constant. This function is then inserted into the free-energy expression (9), which after minimization determines (i) the constant in $f(\rho)$ and (ii) the energy value corresponding to the stable state. It can be shown that, for the case of giant-vortex states, the present approach and that of Ref. 6, which was based on a solution of the nonlinear GL equation, result in the same functional $F(H_{in})$ dependence.

The linearized GL equation for $f(\rho)$ takes the form

$$\hat{L}f=0,\quad \hat{L}=-\frac{1}{\rho}\frac{\partial}{\partial\rho}\rho\frac{\partial}{\partial\rho}+\left(\frac{L}{\rho}-A_0\right)^2-1.\tag{14}$$

The superconducting state starts to develop when the minimal eigenvalue of the operator $\hat{L}$ becomes negative. For the zero angular momentum state, the normal state transforms to the superconducting one with decreasing magnetic field below the nucleation field H_{nuc}. For nonzero angular momentum, the superconducting state appears when we cross either the lower $H_{nuc,l}$ or the upper $H_{nuc,u}$ critical magnetic field, which depends on the disk radius. The eigenvalues and eigenfunctions of the $\hat{L}$ operator are found from

$$\hat{L}f_{n,L}(\rho)=\Lambda_{n,L}f_{n,L}(\rho),\tag{15}$$

where $f_{L,n}(\rho)$ satisfies $\rho(\partial f/\partial\rho)|_{\rho=0}=0$ at the disk center. The index $n=1,2,\ldots$ enumerates the different states for the same L value.

In general, the eigenfunctions of Eq. (15) can be obtained analytically in the case of our step magnetic-field profile. We present the complete calculation in the Appendix for both considered cases. Alternatively, we solve Eq. (15) numerically through the finite difference technique. We put the order parameter on a space grid and find numerically the eigenfunctions and eigenvalues of the operator $\hat{L}$ using the Housholder technique.

We start our analysis with the magnetic-field profile shown in Fig. 1. First, we consider a magnetic dot on top of the center of the disk, i.e., with $R_d=0$ and $R_2=R=6.0\xi$ and

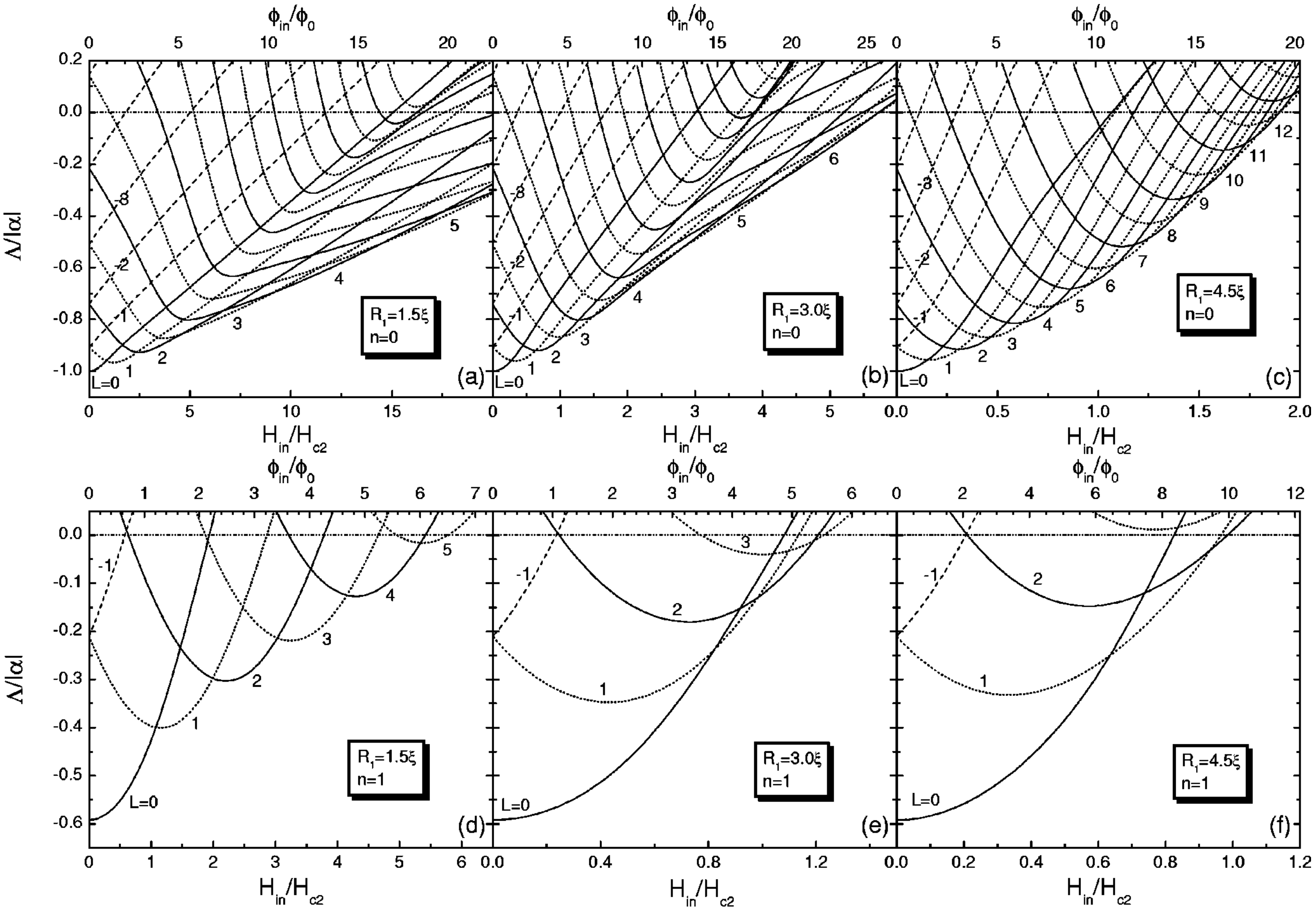

FIG. 2. The magnetic-field dependence of the lowest eigenvalues of the linearized first GL equation for different angular momenta L and for (a) $R_1/\xi=1.5$, (b) $R_1/\xi=3.0$, and (c) $R_1/\xi=4.5$. The corresponding curves for the first radial excited state, i.e., $n=1$, are presented in (d)–(f). The top axis gives the flux through the positive magnetic-field region in units of the flux quantum.

study the influence of R_1, i.e., the width of the positive field region, on the superconducting state.

The magnetic-field dependence of Λ for different angular momenta L is shown in Figs. 2(a–c) for the lowest radial state, i.e., $n=0$, and in Figs. 2(d–f) for the first radial state, i.e., $n=1$ for three different values of R_1. The top axis shows the flux corresponding to the positive magnetic-field region $\phi_{in}=H_{in}\pi R_1^2$, which in dimensionless units becomes $\phi_{in}/\phi_0=(H_{in}/2H_{c2})(R_1/\xi)^2$, where $\phi_0=ch/2e$ is the quantum of flux. All numerical calculations were done for a disk thickness $d/\xi=0.1$, which is within the thin disk approximation. The negative L values (dashed curves in Fig. 2) correspond to antivortices in conventional superconductors. The thin horizontal line gives the $\Lambda=0$ level. From Fig. 2 one notices that with increasing R_1 (1) the eigenvalues Λ of the states with the same L become more negative, (2) the magnetic-field range over which solutions of Eq. (14) can be found decreases, (3) the number of possible solutions decreases, and (4) the $\Lambda(H_{in})$ dependences become more parabolic. The latter can be explained by the fact that increasing R_1 corresponds to a more homogeneous magnetic-field profile inside the disk, i.e., we reach the case considered in Refs. 6 and 20.

For small R_1 the curves L and $L+1$ anticross for sufficiently large L values and consequently the low vorticity states have lower energy even with increasing strength of the magnetic-field profile. E.g., for $R_1/\xi=1.5$ this occurs when $L>4=L^*$ and for $R_1/\xi=3.0$ when $L>5=L^*$. Notice that the slope of Λ for the $L>L^*$ curves is substantially smaller than for the $L\leqslant L^*$ curves in the high-field region. Notice also that the $n=1$ states have a higher Λ value than the $n=0$ states and their energy is also larger than those of the antivortex states for the same vorticity.

In Figs. 3(a–c) the radial dependence of the superconducting density $|\psi|^2$ is shown for $|L|<3$ at $H_{in}=0.75H_{c2}$ for the corresponding profiles of Fig. 2. Notice that, with increasing R_1, the Cooper-pair density near the edge of the sample becomes more nonhomogeneous. The $|L|\neq 0$ states have a vortex sitting in the center of the disk, i.e. $\psi(\rho=0)=0$, which becomes larger with increasing $|L|$. For the situation of Fig. 3(c) there is a narrow, very negative magnetic-field region of $H_{out}/H_{c2}=0.9643$ in the region $4.5<\rho/\xi<6.0$, which leads to a considerable suppression of the Cooper-pair density. For example, the $L=0$ vortex state, i.e., the Meissner state, has a strongly reduced Cooper-pair density for $\rho/\xi>1$. For the excited state $(n,L)=(1,0)$ (dashed curves in Fig. 3) the order parameter vanishes inside the disk and a ring-shaped node in the wave function ψ is formed,[20,21] which leads to a ringlike vortex.

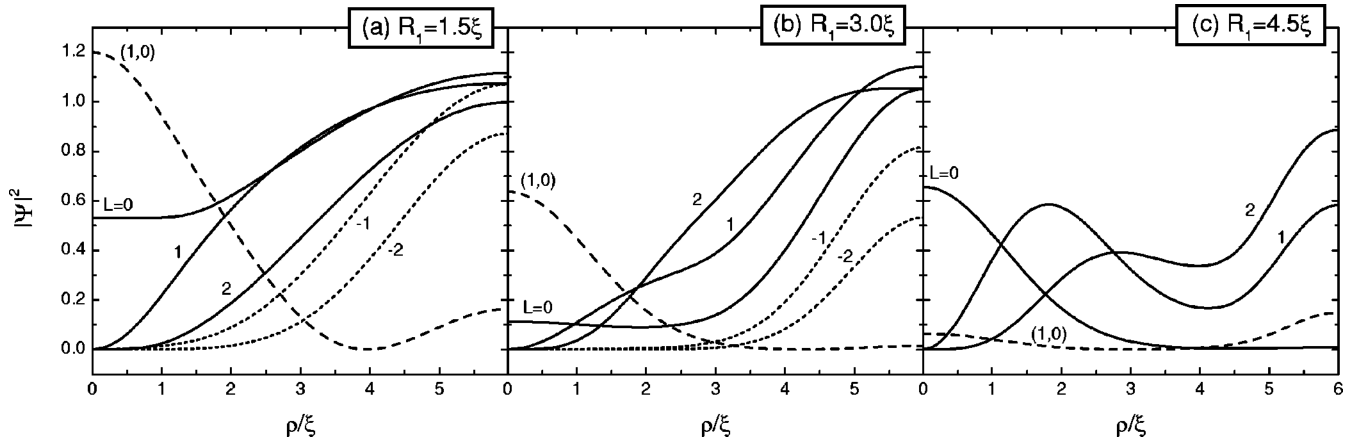

FIG. 3. The Cooper-pair density for the giant-vortex states with angular momenta $L=0,1,2$ (solid curves), the antivortex states $L=-1,-2$ (dotted curves), and the ring vortex state $n=1$, $L=0$ (dashed curve) at the magnetic field $H_{in}=0.75H_{c2}$ for (a) $R_1/\xi=1.5$, (b) $R_1/\xi=3.0$, and (c) $R_1/\xi=4.5$.

The eigenvalues Λ determine the free energy F of the giant-vortex state. For the giant-vortex state we consider only states which lie below the $F=0$ level. In this approximation the order parameter is

$$\psi(\vec{\rho})=\left(-\Lambda\frac{B_{n,L}}{A_{n,L}}\right)^{1/2}f_{n,L}(\rho)\exp(iL\varphi), \tag{16}$$

and the minimal energy value is

$$F=-\Lambda^2\frac{B_{n,L}^2}{A_{n,L}}, \tag{17}$$

where

$$A_{n,L}=\frac{2\pi d}{V}\int_0^R\rho d\rho\, f_{n,L}^4(\rho),\quad B_{n,L}=\frac{2\pi d}{V}\int_0^R\rho d\rho\, f_{n,L}^2(\rho).$$

The dependence of the free energy on the magnetic-field strength of the inner core of the magnetic-field profile, H_{in}, is shown in Figs. 4(a–c) for the angular momenta $|L|<11$ for different values of R_1. The free energy is expressed in units of $F_0=H_c^2V/8\pi$. The highest value of vorticity in this disk is $L=13$ [see Figs. 2(a–c)]. From a comparison of the magnetic-field dependence of $F(H_{in})$ for $R_1/\xi=1.5$ [Fig. 4(a)] with that for $R_1/\xi=4.5$ [Fig. 4(c)] we clearly observe the reduction of superconductivity and the reduction of the maximal possible vorticity with increasing R_1. The envelope of the lowest parts of the curves in Fig. 4 represents the field dependence of the ground-state energy. Notice that the increase of the width of the positive magnetic-field region leads to an increase of the energy of the ground state. With increasing applied field, the $L\rightarrow L+1$ vortex transitions take place at the field where the corresponding curves cross (for example, the $0\rightarrow 1$ transition occurs at $H_{in}=0.8705H_{c2}$ for $R_1/\xi=1.5$). The crossing points are shifted towards lower field values when increasing R_1. The $L\rightarrow L+1$ transitions are of first order and lead to jumps in the magnetization of the sample. Notice that the positive flux captured in the superconducting disk for different L states is not quantized. This is made very clear in the $\phi_{in}-R_1$ diagram presented in Fig. 4(d), which shows the ground-state vortex configurations. Notice that the flux in the positive magnetic-field region has to increase for more than one flux quantum ϕ_0 before the vorticity of the superconducting state can increase for one unit. A similar phenomena was observed earlier for mesoscopic disks and rings in a homogeneous magnetic field.[22] Notice also that for higher L values quantization is slowly restored, and $\Delta\phi$ decreases with enlarging R_1, i.e. the radius of the positive field region.

Following our assumption that the field inside the superconductor equals the external one, we obtain the expression for the superconducting current density:[20]

$$j_{n,L}=\frac{\Lambda_{n,L}B_{n,L}}{A_{n,L}}\left(\frac{L}{\rho}-A_0\right)f_{n,L}^2(\rho), \tag{18}$$

where $\Lambda_{n,L}$ is determined by Eq. (15), and A_0 represents the vector potential of the applied field. The magnetic field due to the supercurrents, neglected in our first-order approximation, is calculated from

$$\vec{\nabla}\times\vec{H}_{sc}=\frac{1}{\kappa^2}\vec{j}. \tag{19}$$

Since the supercurrent has only an azimuthal component, and, is situated only in the superconductor plane, the ρ component of $\vec{H}_{sc}$ can be neglected. Consequently, we obtain

$$H_{sc}(\rho)=-\frac{1}{\kappa^2}\int j_{\varphi}(\rho)d\rho, \tag{20}$$

and the magnetization of the superconductor is then defined as the magnetic field expelled from the superconductor.

$$M=\int\frac{H_{total}-H_0}{8\pi}dV=\frac{d}{4}\int_0^R H_{sc}(\rho)\rho d\rho, \tag{21}$$

where H_0 denotes the applied magnetic field and d is the disk thickness.

The corresponding $M(H_{in})$ curves are given as insets in Figs. 4(a–c). The phase transition from the superconducting

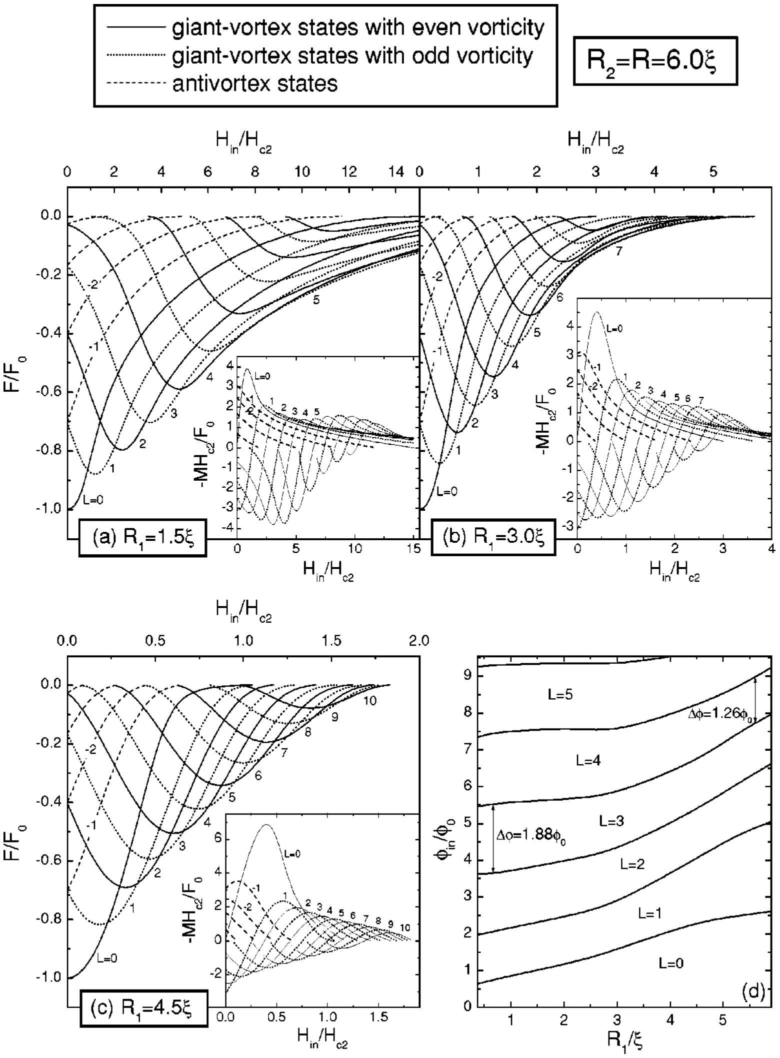

FIG. 4. The free energy of the giant-vortex states with different angular momenta L as a function of the applied magnetic-field in the positive region for (a) $R_1/\xi=1.5$, (b) $R_1/\xi=3.0$, and (c) $R_1/\xi=4.5$. Only the states with $|L|\leqslant 10$ are shown. The insets depict the magnetic field dependence of the disk magnetization for the ground giant-vortex state for different values of the R_1/ξ parameter. (d) gives the positive flux captured in the superconducting disk for the different L ground states as a function of R_1/ξ.

to the normal state is of second order [all curves $F(H_{in})$ reach the $F=0$ line with zero derivative]. The curves $F(H_{in})$ in Fig. 4 which are situated above the ground-state energy correspond to metastable giant-vortex states. With increasing applied field the transition from the Meissner state ($L=0$) to the normal state goes through a set of consecutive first-order transitions between the L and $L+1$ giant vortices, which is finished by a second-order transition to the normal state.

Our next step was to fix the magnetic-field profile (we took $R_d/\xi=0.0$, $R_1/\xi=4.5$, $R_2/\xi=6.0$) and enlarge the

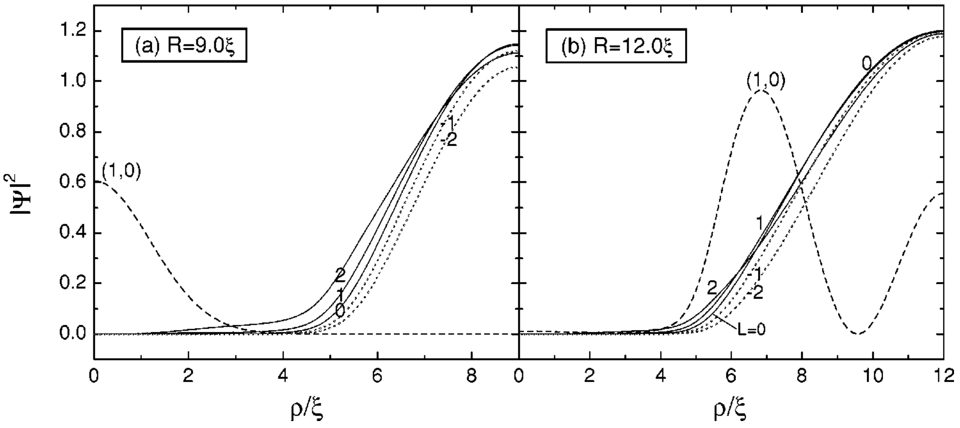

FIG. 5. The Cooper-pair density for the giant-vortex states with angular momenta $L=0,1,2$ (solid curves), the antivortex states $L=-1,-2$ (dotted curves) and the ring-shaped vortex state $n=1$, $L=0$ (dashed curve) at the magnetic field $H_{in}=0.75H_{c2}$ for (a) $R/\xi=9.0$ and (b) $R/\xi=12.0$.

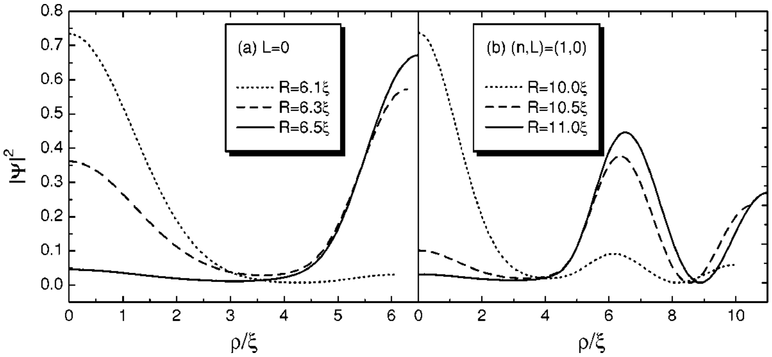

FIG. 6. The Cooper-pair density for (a) the Meissner state ($L=0$) and (b) the ring-shaped vortex state $n=1$, $L=0$ at the magnetic field $H_{in}=0.75H_{c2}$ for different sizes of the superconducting disk.

disk radius R. In Figs. 5(a,b) the radial dependence of the superconducting density $|\psi|^2$ is shown for $|L|<3$ at $H_{in}=0.75H_{c2}$ and for a superconducting disk of radius $R/\xi=9.0$ and 12.0, respectively. One can see that, even for $L=0$, superconductivity in the center of the disk is destroyed, which is opposite to the homogeneous magnetic-field case where $|\Psi|^2$ is maximal at $\rho=0$.[6] The shape of the $L=0$ curve changes drastically and this occurs already for small enlargement of the disk. This transition is shown in Fig. 6(a). By increasing R/ξ from 6.1 to 6.5 the Cooper-pair density in the center of the superconducting disk decreases from 0.73 to 0.03. Furthermore, in Fig. 5(b) we see also qualitative changes in the Cooper-pair density of the excited state $(n,L)=(1,0)$ (dashed curve). Now the order parameter vanishes twice inside the disk and a double ringlike vortex is formed. This transition is shown in Fig. 6(b) with increasing disk size from $R/\xi=10.0$ to 11.0.

The dependences of the free energy on the magnetic field H_{in} for different sizes of the superconducting disk are shown in Figs. 7(a–d). Notice that there are large differences in comparison with the previous cases. We still have the $L\rightarrow L+1$ transitions, which are of first order and which lead to jumps in the magnetization of the sample [see Figs. 8(a–c)]. With increase of the applied field the transition from the Meissner state ($L=0$) to the vortex state goes through consecutive first-order transitions and is finished by a first-order transition *back to the* $L=0$ *state*, sometimes with an intermediate $L=1$ state. For $R/\xi=9.0$ we have $0\rightarrow1\rightarrow2\rightarrow3\rightarrow1\rightarrow0$ transitions, for $R/\xi=12.0$ we have $0\rightarrow1\rightarrow2\rightarrow1\rightarrow0$, and for $R/\xi=18.0$ only $0\rightarrow1\rightarrow0$. Moreover, for a sufficiently large disk [see Fig. 7(d), which corresponds practically to the $R/\xi\rightarrow\infty$ situation] we have no first-order transitions but only the Meissner state as the ground state. The reason is that for $R/\xi\rightarrow\infty$ the nonzero magnetic-field region is limited (relatively) to a small area and we can always define a circle with radius ρ sufficiently large where the su-

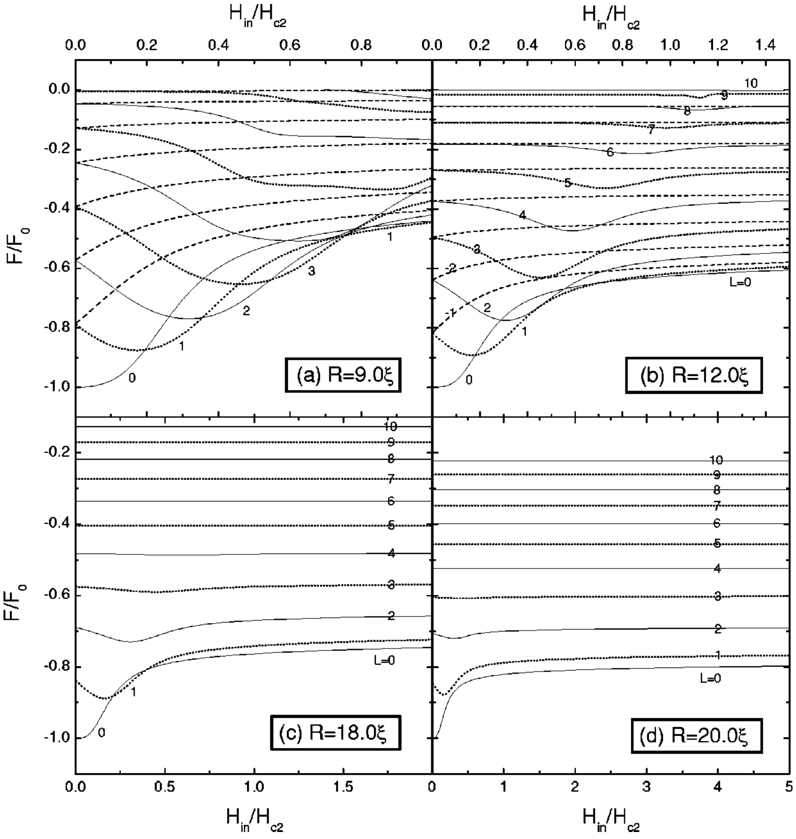

FIG. 7. The free energy of the giant-vortex states with different angular momenta L as a function of the applied magnetic field for (a) $R/\xi=9.0$, (b) $R/\xi=12.0$, (c) $R/\xi=18.0$, and (d) $R/\xi=20.0$, with $R_1/\xi=4.5$ and $R_2/\xi=6.0$. Dashed curves represent the energy of the antivortex states.

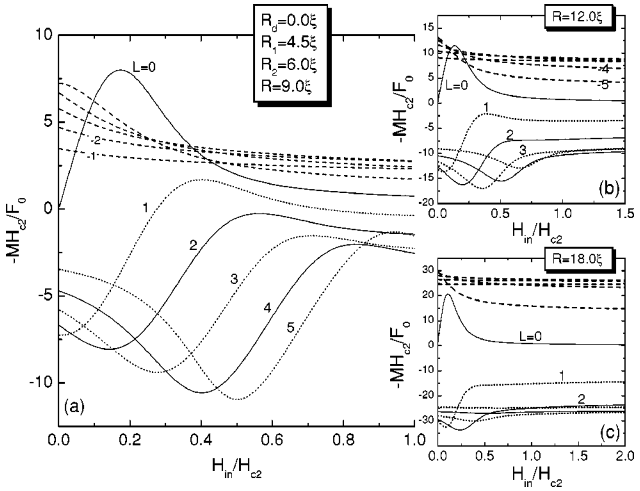

FIG. 8. The magnetic-field dependence of the disk magnetization for the ground giant-vortex state corresponding to the states in Fig. 7, for (a) $R/\xi=9.0$, (b) $R/\xi=12.0$, and (c) $R/\xi=18.0$.

perconducting current is zero and, consequently one must have $L=0$. But, this Meissner state is qualitatively different from the "usual" one. The radial distribution of the Cooper-pair density is extremely inhomogeneous and superconductivity is strongly suppressed in the interior of the disk [see Figs. 5(b) and 6(a)]. Notice that this kind of *reentrant* behavior differs from those previously found in rings with large radius in a homogeneous magnetic field [multivortex(L) $\rightarrow$giant(L)$\rightarrow$multivortex($L+1$)$\rightarrow\cdots$) (Ref. 22) or in disks with enhanced surface superconductivity [giant(L) $\rightarrow$multivortex(L)$\rightarrow$giant(L)].[20] In our case, we have a reentrance of the *total vorticity* and it happens due to the spatial inhomogeneity of the magnetic field.

IV. MULTIVORTEX STATES

It is well known that for sufficiently large disks the giant-vortex state can break up into multivortices.[7–9] In our analysis, we considered different field profiles and disk geometries to investigate the properties of this transition. For smaller disks, the confinement effect dominates and we found that only the giant-vortex states are stable, and possible multivortex states, if they exist, have always larger energies. In order to investigate such structures in our case we use the method proposed by Schweigert *et al.*[7] and Palacios[8,9] and extend it to determine the stability of the different multivortex configurations as proposed in Ref. 20. Following Refs. 7, 8, and 23 the order parameter of the multivortex state is written as a linear combination of eigenfunctions of the linearized GL equation (14),

$$\psi(\vec{\rho})=\sum_{L_j=0}^{L}\sum_{n=0}^{\infty}C_{n,L_j}f_{n,L_j}(\rho)\exp(iL_j\varphi), \tag{22}$$

where L is, in the homogeneous magnetic-field case, the value of the effective total angular momentum, which is equal to the number of vortices in the disk, and n enumerates the different radial states for the same L_j. Later on, we will see that for our inhomogeneous magnetic-field case the assignment of the total vorticity can be tricky.

Substituting Eq. (22) in the free-energy expression (9) we obtain F as a function of the complex parameters $\{C_{n,L_j}\}$. Minimization of F with respect to these parameters allows us to find the equilibrium vortex configurations, and to determine their stability. We use the procedure described in Refs. 20 and 23 with full consideration of combinations of vortex configurations with different radial states.

We begin our analysis with states built up by only two components in Eq. (22). This brings quantitative bounds to our calculation but, nevertheless, facilitates the physical insight into the problem and will give the correct qualitative behavior of the system under consideration. As we will see later, the accounting of more components in Eq. (22) brings only minor quantitative corrections to the results of the two-component analysis.

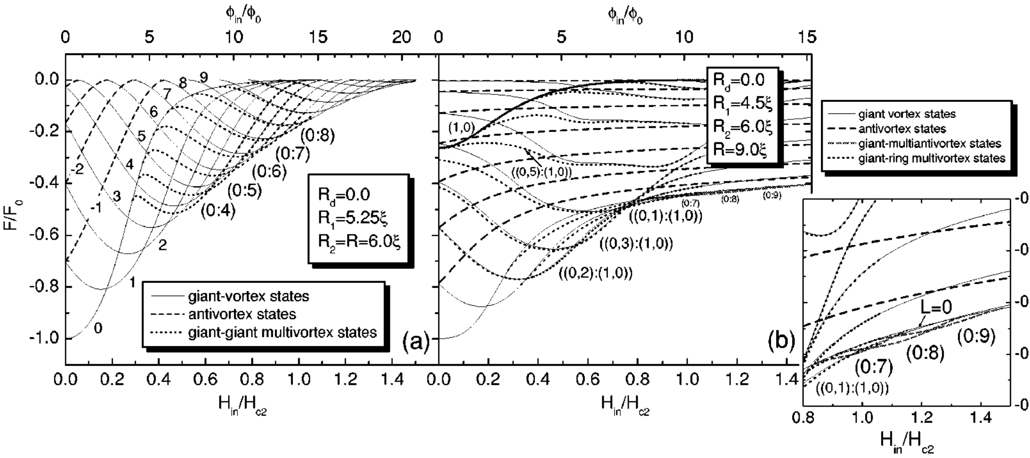

FIG. 9. The free energy of the giant-vortex states with different angular momenta L as a function of the external magnetic field for (a) $R_1/\xi=5.25$, $R_2/\xi=R/\xi=6.0$, and (b) $R_1/\xi=4.5$, $R_2/\xi=6.0$, $R/\xi=9.0$. The inset shows an enlargement of a part of this figure. Dashed curves illustrate the energy of the antivortex states. In (a) dotted curves represent the giant-giant multivortex states while in (b) dotted curves depict the free energy of the giant-ring multivortex states, and the short dotted curves correspond to the giant-giant (giant-multiantivortex) states. Thick solid curve illustrates the energy of the ring vortex state, i.e., $(n,L)=(1,0)$.

The free energy of a two-component state built out of states (n_1,L_1) and (n_2,L_2) is

$$F=C^4_{n_1,L_1}A_{n_1,L_1}+C^4_{n_2,L_2}A_{n_2,L_2}+4C^2_{n_1,L_1}C^2_{n_2,L_2}A_{n_1,n_2,L_1,L_2}+2\Lambda_{n_1,L_1}C^2_{n_1,L_1}B_{n_1,L_1}+2\Lambda_{n_2,L_2}C^2_{n_2,L_2}B_{n_2,L_2}, \tag{23}$$

where

$$A_{n_i,L_i}=\frac{2\pi d}{V}\int_0^R\rho d\rho\, f^4_{n_i,L_i}(\rho),$$

$$A_{n_1,n_2,L_1,L_2}=\frac{2\pi d}{V}\int_0^R\rho d\rho\, f^2_{n_1,L_1}(\rho)f^2_{n_2,L_2}(\rho),$$

$$B_{n_i,L_i}=\frac{2\pi d}{V}\int_0^R\rho d\rho\, f^2_{n_i,L_i}(\rho).$$

One should notice that we leave the possibility of combination of states with different radial states, i.e. n_1 and n_2. Although, in general, C_{n_i,L_i} is a complex number, for our two-component state C_{n_i,L_i} is a real number. Minimization of Eq. (23) with respect to C_{n_1,L_1} and C_{n_2,L_2} gives for the multivortex states

$$C^{(0)}_{n_1,L_1}=\pm\left(\frac{-\Lambda_{n_1,L_1}A_{n_2,L_2}B_{n_1,L_1}+2\Lambda_{n_2,L_2}A_{n_1,n_2,L_1,L_2}B_{n_2,L_2}}{A_{n_1,L_1}A_{n_2,L_2}-4A^2_{n_1,n_2,L_1,L_2}}\right)^{1/2}, \tag{24}$$

$$C^{(0)}_{n_2,L_2}=\pm\left(\frac{-\Lambda_{n_2,L_2}A_{n_1,L_1}B_{n_2,L_2}+2\Lambda_{n_1,L_1}A_{n_1,n_2,L_1,L_2}B_{n_1,L_1}}{A_{n_1,L_1}A_{n_2,L_2}-4A^2_{n_1,n_2,L_1,L_2}}\right)^{1/2},$$

and inserting these expressions into Eq. (23) leads to *the energy of the multivortex state*

$$F_{n_1,n_2,L_1,L_2}=\frac{-\Lambda^2_{n_1,L_1}A_{n_2,L_2}B^2_{n_1,L_1}-\Lambda^2_{n_2,L_2}A_{n_1,L_1}B^2_{n_2,L_2}+4\Lambda_{n_1,L_1}\Lambda_{n_2,L_2}A_{n_1,n_2,L_1,L_2}B_{n_1,L_1}B_{n_2,L_2}}{A_{n_1,L_1}A_{n_2,L_2}-4A^2_{n_1,n_2,L_1,L_2}}. \tag{25}$$

The corresponding conditions for the stability of the vortex state are

$$\frac{\partial^2F}{\partial C^2_{n_1,L_1}}=\frac{8A_{n_1,L_1}(-\Lambda_{n_1,L_1}A_{n_2,L_2}B_{n_1,L_1}+2\Lambda_{n_2,L_2}A_{n_1,n_2,L_1,L_2}B_{n_2,L_2})}{A_{n_1,L_1}A_{n_2,L_2}-4A^2_{n_1,n_2,L_1,L_2}}>0, \tag{26}$$

$$\frac{\partial^2F}{\partial C^2_{n_2,L_2}}=\frac{8A_{n_2,L_2}(-\Lambda_{n_2,L_2}A_{n_1,L_1}B_{n_2,L_2}+2\Lambda_{n_1,L_1}A_{n_1,n_2,L_1,L_2}B_{n_1,L_1})}{A_{n_1,L_1}A_{n_2,L_2}-4A^2_{n_1,n_2,L_1,L_2}}>0,$$

$$\frac{\partial^2F}{\partial C^2_{n_1,L_1}}\frac{\partial^2F}{\partial C^2_{n_2,L_2}}-\left(\frac{\partial^2F}{\partial C_{n_1,L_1}\partial C_{n_2,L_2}}\right)^2=\frac{64(-\Lambda_{n_1,L_1}A_{n_2,L_2}B_{n_1,L_1}+2\Lambda_{n_2,L_2}A_{n_1,n_2,L_1,L_2}B_{n_2,L_2})}{A_{n_1,L_1}A_{n_2,L_2}-4A^2_{n_1,n_2,L_1,L_2}}\times(-\Lambda_{n_2,L_2}A_{n_1,L_1}B_{n_2,L_2}+2\Lambda_{n_1,L_1}A_{n_1,n_2,L_1,L_2}B_{n_1,L_1})>0.$$

In our analysis we investigated the influence of the width of the positive field region and radius of the disk on the phase diagram, and especially on the stability of the multivortex states. For small values of R_1/ξ these multivortex states are always metastable. However, with enlarging R_1/ξ these states can obtain lower energy. The energies of the equilibrium vortex states are plotted in Fig. 9(a) for $R_1/\xi=5.25$ and $R_2/\xi=R/\xi=6.0$ and in Fig. 9(b) for $R_1/\xi=4.5$ and $R_2/\xi=6.0$ with a larger disk radius $R/\xi=9.0$. The giant-vortex states are given by solid curves, antivortex states by dashed, and the multivortex states (dotted curves) by $(L_1:L_2)$, i.e., the angular momentum values they are composed of. As expected, when enlarging the disk, multivortex states become more stable and, moreover, in Fig. 9(b), we observe the existence of multivortices as a combination of a giant vortex and a ringlike vortex. These states have surprisingly low energy and become the ground state for a specific range of magnetic field. Furthermore, when increasing the field, we observe a phase transition between this giant-ring and giant-giant multivortex states, when another type of multivortices becomes the ground state. The giant-ring multivortex states with lowest energy are given in Fig. 9(b) by the quantum numbers $((n_1,L_1):(n_2,L_2))$. It should be noted that

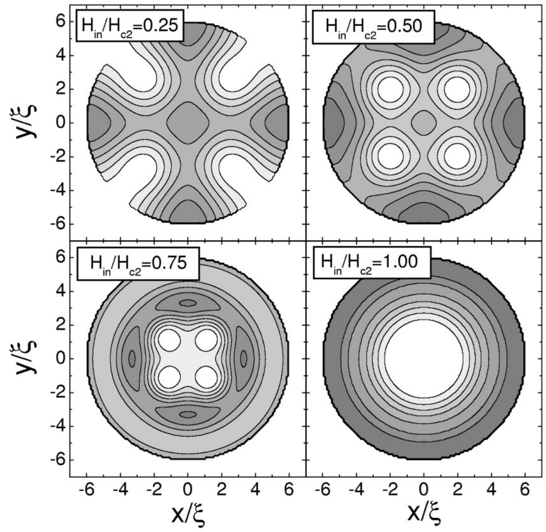

FIG. 10. Transition between two giant-vortex states shown through the contour plots of the superconducting wave-function density for the $(0{:}4)$ giant-giant multivortex state for different values of the magnetic field in the positive field region (corresponding to the magnetization of the dot).

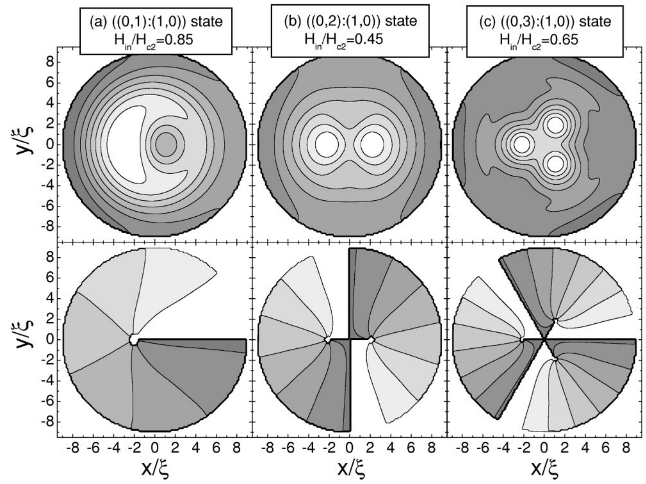

FIG. 11. Contour plots of the superconducting density for the ground state and the corresponding phase contour plots [see Fig. 9(b)] for different values of the magnetic field in the positive region.

there are many other metastable combinations possible, which are not shown in the figures.

As shown in Fig. 9, with increasing R_1/ξ and the size of the superconducting disk, the multivortices become more stable and they can even become the minimum of the $F(C_{n_1,L_1},C_{n_2,L_2})$ function. We focus our attention on Fig. 9(a). The solid and dashed curves represent the giant-vortex and antivortex states, respectively. The dotted curves are the energies of the multivortices. For example, let us follow the $L=0$ curve which splits into the $(0{:}4)$ multivortex state at $H_{in}/H_{c2}=0.28$ and with further increase of the field becomes another giant-vortex state, but now with $L=4$, at $H_{in}/H_{c2}=1.0$. The concomitant change of the Cooper-pair density is illustrated in Fig. 10. Vortices enter the disk from the boundary and move to the middle with increasing field, and join into a giant vortex again.

For a fixed magnetic-field profile and with increasing size of the superconducting disk, we obtain a variety of different superconducting states. Let us discuss the giant-ring configurations first. We observe transitions between the giant-vortex and multivortex states with the *same* vorticity. The contour plots of the $|\psi|^2$ distribution for different multivortex states as ground states [((0,1):(1,0)), ((0,2):(1,0)), ((0,3):(1,0))] are shown in Figs. 11(a–c) for a magnetic-field profile with $R_1/\xi=4.5$, $R_2/\xi=6.0$, and $R/\xi=9.0$, for different values of H_{in} (dark regions correspond to high density and white regions to low density). The most interesting result we obtain is for the ((0,1):(1,0)) combination. This configuration becomes the ground-state configuration for $H_{in}/H_{c2}=0.75$. Surprisingly, the contour plot of the $|\psi|^2$ distribution is not circular symmetric—there is one vortex positioned off-center. In the lower part of the same figures we give the corresponding contour plots of the phase of the superconducting wave functions. The contour plot of the phase also nicely illustrates the off-center location of the vortex. For the two other cases, more vortices are present which are located on a ring centered around the center of the superconducting disk. The giant-ring multivortex state can be seen as a transition between (1,0) and (0,5) states [see Fig. 9(b)]. As a function of the magnetic field we start from a ring vortex, for $H_{in}/H_{c2}=0.03$, this state splits into a giant-ring vortex state, and finally, for $H_{in}/H_{c2}=0.98$ we obtain a giant-vortex state. This remarkable phenomenon is illustrated in Fig. 12.

However, giant-giant vortex combinations show completely different behavior. As shown in Fig. 9(b) with increasing magnetic field H_{in}, combinations $(0{:}7)$, $(0{:}8)$, $(0{:}9)$, etc. become the ground state. In the contour plot of the $|\psi|^2$ distribution we observe single vortices which are arranged on a ring with a low-density area situated in the center of the disk [see Figs. 13(a–c)]. This central area is associated with a giant vortex, and encircling it leads to a

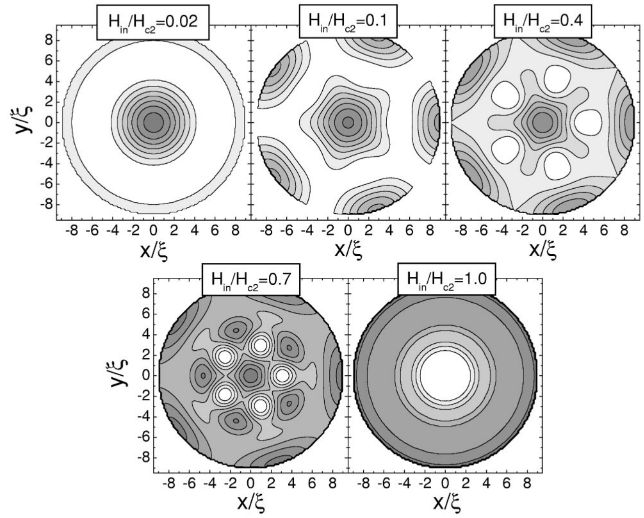

FIG. 12. Contour plot of the superconducting density for the ((0,5):(1,0)) giant-ring multivortex state [see Fig. 9(b)] for different values of the applied magnetic field.

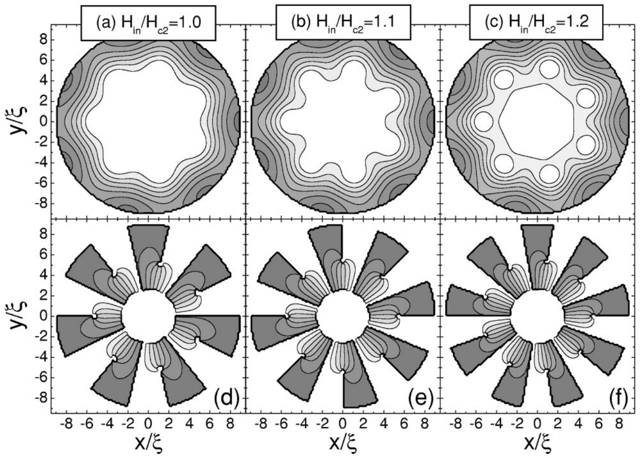

FIG. 13. (a)–(c) Contour plots of the superconducting density for the (0:7), (0:8), and, (0:9) giant-multiantivortex states, respectively, for different values of the magnetic field H_{in}; (d)–(f) the corresponding contour plots of the phase of the superconducting wave-function density. Notice that the phase near the boundary is near 0 or 2π but due to the finite numerical accuracy it oscillates between $2\pi-\varepsilon$ and $2\pi+\varepsilon$, where $\varepsilon\sim10^{-5}$.

phase change showing the vorticity 7. Figure 13(d) shows the contour plot of the corresponding phase with seven *antivortices* arranged in a circle around the giant vortex and the *total* vorticity is $L=0$. Figures 13(e) and 13(f) correspond, respectively, to the giant-vortex states with vorticity 8 and 9 where, respectively, 8 and 9 antivortices are located between the giant vortex and the boundary. Notice that the Cooper-pair density for the $L=0$ state for this disk geometry ($R_1/\xi=4.5$, $R_2/\xi=6.0$, $R/\xi=9.0$) shows a similar behavior with a low-density area in the center of the disk [see Fig. 5(b)]. It is obvious that enlarging the superconducting disk enhances the influence of the negative part of the steplike magnetic field.

One could notice that a similar arrangement of the vortices was found in ring structures in the presence of a homogeneous magnetic field, where the giant vortex with $L>1$ is surrounded by single vortices.[22] However, in our system with an inhomogeneous magnetic field, antivortices surround the central giant vortex. Furthermore, in our case, when multi-antivortices are involved, the total vorticity of the giant-giant multivortex state is equal to the lowest vorticity of the giant-vortex states that compose the multivortex, contrary to the situation encountered in Ref. 22.

One more result should be noted. Following the ground-state free-energy diagram [Fig. 9(b)] we notice that the total vorticity does not change uniformly ($0\rightarrow1\rightarrow2\rightarrow3\rightarrow1\rightarrow0$) and that the jumps in vorticity $|\Delta L|$ are not always equal to 1. This differs from Ref. 24 where it was claimed that the lowest barriers are those between the L and $L\pm1$ states. We found that the $L\rightarrow L\pm1$ transitions take place in disks for a small maximum value of vorticity or at magnetic fields close to the superconducting-normal state transition point. Between these two limiting regimes $L\rightarrow L\pm N$ transitions are possible with $|\Delta L|=N>1$. Our results are also in agreement with Ref. 25 where it was found numerically that several vortices can enter (or exit) at once for disks with sufficiently large radius. In Sec. III, where we investigated the influence of R_1/ξ (with $R_2/\xi=R/\xi=6.0$) we only found $L\rightarrow L+1$ transitions.

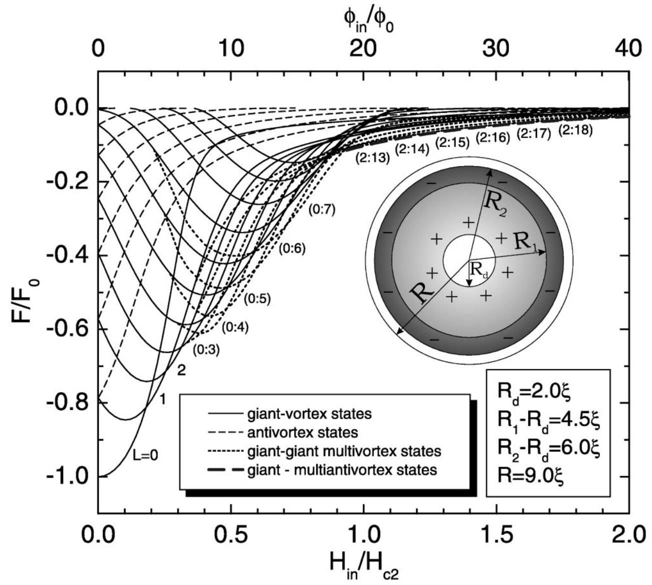

FIG. 14. The free energy of the giant-vortex states with different angular momenta L as a function of the external magnetic field for $R_d=2.1\xi$, $R_1=6.6\xi$, $R_2=8.1\xi$, $R/\xi=9.0$. Dashed curves depict the antivortex states and dotted curves represent the free energy of the giant-giant multivortex states. A bird's view of the magnetic-field profile is given in the inset.

In order to show the complexity of the system under study, we investigated one more field profile, the one shifted from the center of the disk, i.e., a ring magnetic field. We keep all parameters from the previous case, and shift the field by $R_d=2.0\xi$ ($R_1-R_d=4.5\xi$, $R_2-R_d=6.0\xi$, $R/\xi=9.0$) towards the disk edge (a top view of this profile is given schematically in the inset of Fig. 14). As shown in Fig. 14, with $R_d\neq0$ the multivortices become more stable and for $H_{in}/H_{c2}>0.31$ they are the ground state. The solid curves represent the giant-vortex states, dashed curves denote the energy of the antivortex states, while the dotted curves correspond to the energy of the multivortices. Since giant-vortex states show similar, reentrant behavior as for the $R_d=0$ case, the multivortex configurations behave analogously. Giant-giant multivortex states dominate the free-energy diagram, while the giant-ring combinations are present only as metastable states and are not shown in Fig. 14. However, one should notice the presence of giant-multiantivortex states, again strongly correlated with reentrant behavior. The complete equilibrium phase diagram for $R_d\in[0.3,3]$ is given in the following section.

We checked that for the disk parameters which we used, an increase of the number of components in Eq. (22) does not lead to different vortex configurations in the ground state. In order to investigate the region of stability of multivortex states in the above analysis, we took the order parameter as a linear combination of three components in Eq. (22) and minimized the free energy with respect to the three variational parameters C_{L_i}. The giant-vortex and multivortex

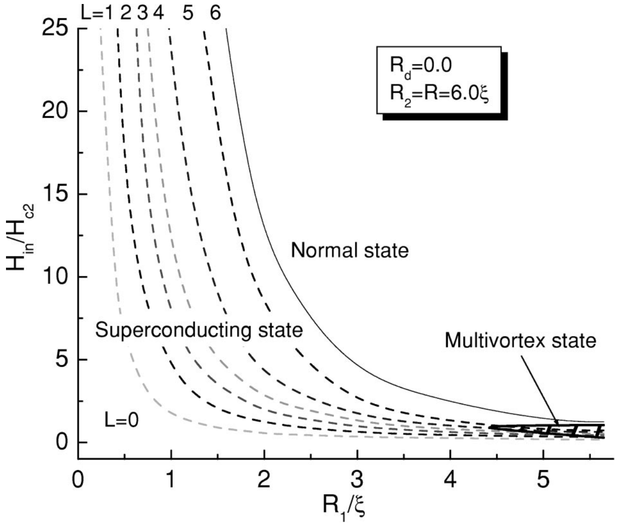

FIG. 15. The H_{in}-R_1 equilibrium vortex phase diagram for a thin superconducting disk with $R_d/\xi=0.0$, $R_2/\xi=6.0$, and $R/\xi=6.0$. Dashed curves indicate transitions between different giant-vortex states and the thick shaded area denotes the multivortex region. The normal/superconducting state transition is given by the thin solid curve.

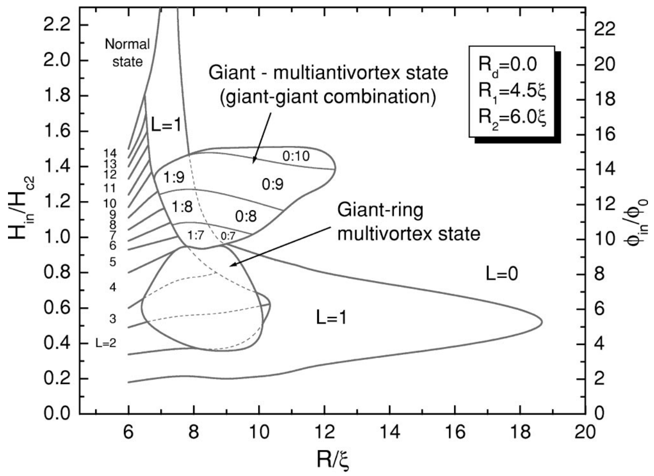

FIG. 16. The H_{in}-R phase diagram for the ground state of a thin superconducting disk with $R_d/\xi=0.0$, $R_1/\xi=4.5$, and $R_2/\xi=6.0$. Solid curves indicate transitions between different vortex states including multivortex (giant-multiantivortex and giant-ring) regions. Dashed curves denote the transitions between different metastable giant-vortex states.

states considered before correspond to the extremum points of the $F(C_{L_1},C_{L_2},C_{L_3})$ function. This analysis has shown that accounting of the third component in Eq. (22) gives all states obtained in the two-component consideration. Additionally, it results in (1) possible reducing of the region of existence of metastable multivortex states at the low magnetic-field limit, (2) appearance of additional unstable states corresponding to the saddle points of the $F(C_{L_1},C_{L_2},C_{L_3})$ function, and (3) no new vortex configurations in the ground state. We did a similar investigation using the numerical approach of Schweigert and Peeters.[23] This was done for five-component vortex configurations and the same results were obtained. Using two different approaches, for three and five components, no new ground-state configurations are found. Moreover, energies of the same states found in both analyses for different number of components differ by less than 0.2%. Because all multivortex configurations considered in this paper are in the ground state, or near it, we conclude that the two components in Eq. (22) are enough to describe the vortex structure in our system.

V. $H_{in}-R$ PHASE DIAGRAMS

First, we investigate the influence of the width of the positive magnetic-field region on the different vortex configurations. Having the free energies of the different giant-vortex configurations for several values of R_1/ξ, we construct an equilibrium vortex phase diagram. Figure 15 shows this phase diagram for a superconducting disk with radius $R=6.0\xi$ and thickness $d=0.1\xi$, where we took $R_2=R$. The dashed curves indicate where the ground state of the free energy changes from one L state to another and the solid curve gives the normal/superconducting transition. Notice that the superconducting/normal transition moves towards lower fields with increasing radius of the positive field region. Also notice that we do not have any negative L (antivortex) state as a ground state, not even when the negative field area is much larger than the positive one.

As shown in the preceding section, an increase of R_1/ξ is able to bring the energy of the multivortex states below those of the giant-vortex states and they can become the ground state [see Fig. 9(a)]. In our phase diagram, the area bounded by the thick curves denotes the region of existence of the giant-giant multivortex states as ground state. One can see that, with enlargement of the positive field region, ground-state multivortices appear for $R_1/\xi=4.42$ and $H_{in}/H_{c2}=0.91$. Further increase of R_1/ξ broadens this *multivortex area* to almost the whole superconducting region. These multivortex states consist of vortices in a ring structure, and the total vorticity equals the highest vorticity of the giant-vortex states involved (at least in the case where there are no antivortices present).

In order to show that the stabilization of the multivortex states due to an inhomogeneous magnetic field is not peculiar to the $R=6.0\xi$ disks, we repeated the previous calculations for a larger superconducting disk. Furthermore, we investigated in detail the phenomena shown in the preceding section (Figs. 11–13).

The effect of the size of the superconducting disk on the phase diagram is illustrated in Fig. 16. The parameters considered are $R_d/\xi=0.0$, $R_1/\xi=4.5$, and $R_2/\xi=6.0$. The solid lines indicate where the ground state of the free energy changes from one state to another (either giant-vortex or multivortex state) and dashed lines correspond to transitions between different giant-vortex states as metastable states. One can clearly see the reentrant behavior. For example, for $R/\xi=9.0$ we observe the change of the total vorticity as $L=0\rightarrow1\rightarrow2\rightarrow3\rightarrow1\rightarrow0$. The $L=0$ and $L=1$ states as ground state cover the largest part of the phase diagram. With increasing disk size, all other giant-vortex states are strongly suppressed in favor of the various multivortex states. Different giant-vortex states are present as the ground state for small disk sizes but with increase of disk size, is-

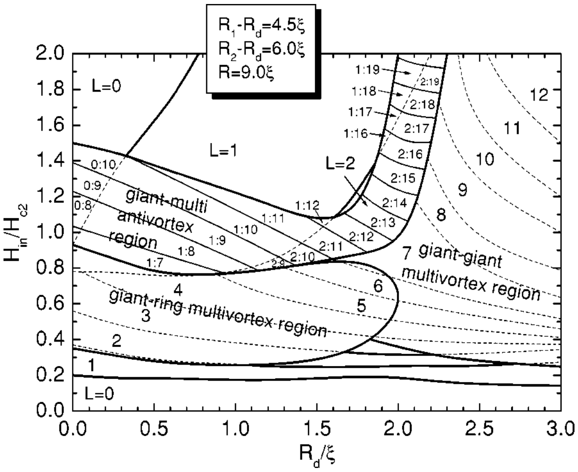

FIG. 17. The H_{in}-R_d phase diagram for the ground state of a thin superconducting disk with $R_1 - R_d = 4.5\xi$ and $R_2 - R_d = 6.0\xi$, i.e., a ring inhomogeneous magnetic-field distribution. The same curve convention is used as in Fig. 16.

lands with different multivortex configurations (giant-ring and giant-giant multivortex states) dominate the ground-state diagram. Precisely, for $R = 6.38\xi$, giant-ring multivortex states appear as the ground state, and for $R = 6.77\xi$ we obtain the giant-giant multivortex states as the ground state. In the previous diagram in Fig. 15 we have shown the existence of the giant-giant multivortex states as the ground state for $R = 6.0\xi$. With a slight increase of the disk size, these states become metastable, and with further enlargement of the superconducting disk, they become the ground state again. However, these states are different from the previous ones and in the contour plots of the Cooper-pair density of these giant-giant multivortex states (see Fig. 13) we found a giant-vortex state in the middle of the superconducting disk surrounded by antivortices, and where the total vorticity is now equal to the lowest vorticity of the giant-vortex states that the multivortex consists of. For $R > 12.33\xi$, the multivortex states become metastable again and the $L = 0$ and $L = 1$ states become the only ground states. Moreover, for $R > 19.34\xi$ we have the Meissner state for all values of the applied magnetic field.

To present the complexity and excitement in this study, we give one more diagram. As shown before, moving the steplike field profile along the radius of the superconducting disk, i.e., a ring magnetic-field profile as in the case of a current loop, stabilizes the giant-giant multivortex states as the ground state. In Fig. 17, we present the phase diagram as a function of R_d. The parameters of the magnetic-field profile are $R_1 - R_d = 4.5\xi$, $R_2 - R_d = 6.0\xi$, and $R/\xi = 9.0$. Thick solid curves indicate the transitions between different vortex states and dashed lines denote the transitions between metastable giant-vortex states. The reentrant behavior, as in previous case, is clearly visible. The most important result is that the multivortex states dominate this diagram. Moreover, we have both types of multivortices, i.e., giant-giant and giant-ring, as stable and ground state, and with shifting the field profile towards the disk periphery, giant-giant multivortex configurations cover most of the superconducting region. The giant-giant multivortex states in this case appear both as states with no anti-vortices present, and as giant-multiantivortex states. Following the transition lines, a correspondence between different giant-multiantivortex states (L_1:L_2) can be seen: L_2 remains the same, while L_1 increases from 0 to 2. As one can see, the latter is strongly correlated with reentrant behavior. In the rest of the diagram, the multivortex states with the "classical" geometry (both giant-giant and giant-ring) dominate. However, a difference between those two states exists. As shown in Fig. 12, in the case of a giant-ring state, vortices are preferentially distributed within a ring-shaped lower-density area. Further, considering the high-density areas at the disk periphery, a shift in phase of $\Delta\theta = \pi/L$ is observed, in comparison with the corresponding giant-giant state (see, for example, Fig. 10), where L is the total vorticity. Although these states have a different origin, sometimes they can exhibit a similar distribution of vortices, but the phase is always able to distinguish between them.

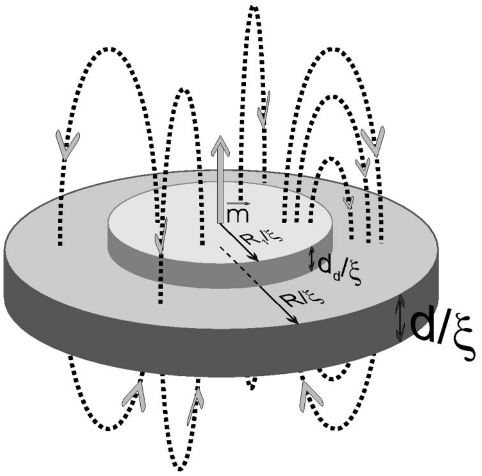

FIG. 18. The configuration: a superconducting disk with radius R and thickness d with a ferromagnetic dot with radius R_1 and thickness d_d, which is placed on top of it.

VI. COMPARISON WITH REAL MAGNETIC-FIELD PROFILE

As emphasized before, our steplike field model can be considered as a simplification of the magnetic-field profile of a ferromagnetic dot (see solid curve in Fig. 1), as shown schematically in Fig. 18. In this case, the radius of the dot corresponds to R_1, and R_2 is always equal to R. The magnetic field and vector potential were calculated through the numerical integration of

$$H_z(\rho,z) = m_z \int_0^{R_1} dr' \frac{4r'(z'-z)}{\sqrt{(r'-\rho)^2+(z'-z)^2}[(r'+\rho)^2+(z'-z)^2]} \times E\left[-\frac{4r'\rho}{(r'+\rho)^2+(z'-z)^2}\right]\Bigg|_{z_0'}^{z_1'} \tag{27}$$

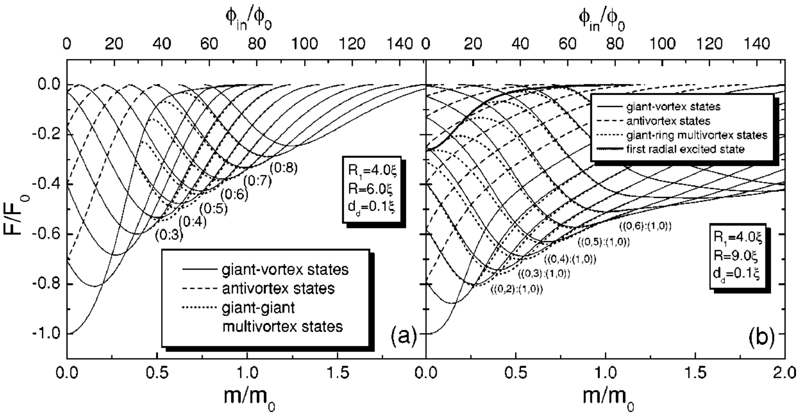

FIG. 19. The free energy of different vortex states as a function of the magnetic moment of the ferromagnetic dot with (a) $R_1/\xi=4.5$, $R_2/\xi=R/\xi=6.0$ and (b) $R_1/\xi=4.5$, $R_2/\xi=R/\xi=9.0$. In (a), dotted curves depict the free energy of the giant-giant multivortex states, while in (b) dotted curves denote giant-ring states. The bold curve gives the energy of the ring vortex state, i.e., $(n,L)=(1,0)$. The energy of the antivortex states is given by the dashed curves.

and

$$A_\varphi(\rho,z)=\frac{1}{\rho}\int_0^\rho rH_z(r,z)dr,$$

where m_z denotes the magnetic moment of a dot directed along the z axis, R_1 is the radius of the dot, z_0' gives the distance from the plane of interest, and $d_d=z_1'-z_0'$ is the thickness of the dot. $E(x)$ is the complete elliptic integral of the second kind. The calculations were done for $z\rightarrow 0$, which allowed us to neglect the radial component of the magnetic field.

In order to examine the quality of our previous model we repeated the analysis from previous sections. First, we enlarge R_1, i.e., the radius of the magnetic dot, investigating the influence of the magnetic field on the vortex structure and especially on the stability of the multivortex states, and second, we studied the vortex configurations resulting from an increase of the superconducting disk size.

For small values of R_1/ξ the multivortex states are always metastable. However, by enlarging this parameter these states lower in energy. The energies of the equilibrium vortex states, as a function of the magnetic moment of the dot measured in units of $m_0=H_{c2}$, are plotted in Fig. 19(a) for radius of the dot $R_1/\xi=4.0$ and $R/\xi=6.0$ and in Fig. 19(b) for $R_1/\xi=4.0$ with a larger disk radius $R/\xi=9.0$. Dashed curves correspond to antivortex states and dotted curves represent the energy of the multivortex states. The giant-giant multivortex states are given by $(L_1{:}L_2)$, i.e., the angular momentum values they are composed of, and the giant-ring multivortex states with lowest energy are given in Fig. 19(b) by $((n_1,L_1){:}(n_2,L_2))$. It should be noted that there are many other metastable combinations possible, which are not shown in the figures. Notice from Fig. 19(a) that the results are qualitatively similar to the results obtained with our step magnetic-field model (see Fig. 9). The difference is caused by the fact that part of the negative magnetic flux does not penetrate the superconducting disk. Because the positive field region in the center dictates the behavior of the phase diagram even when the total flux is zero [see, for example, Fig. 9(a)], we obtain very similar results with the real magnetic-field profile, but with an increased number of possible superconducting states. However, increasing the size of the superconductor brings some qualitative changes. First, it is clear from Fig. 19(b) that there is no reentrant behavior, and, second, no giant-giant multivortex configurations are ground state. But, this was expected since in our model field profile the whole magnetic flux is trapped in the center of the disk, with total flux equal to zero. For the real profile, the total flux would be zero if our disk is infinitely extended, and, more importantly, the flux is now spread over the whole disk area. Naturally, smaller magnetic dots in combination with large superconductors would make the correspondence better, since most of the flux would be captured inside the disk.

A similar discussion holds for the results for the real magnetic-field profile of a current loop placed on top of a superconductor. This field profile (solid curve) is compared with our model in Fig. 20 (thick dashed curve). The magnetic field and vector potential were calculated numerically from

$$H_z(\rho,z)=\frac{Ik}{4\sqrt{R_1\rho}}\left[\frac{R_1^2-\rho^2-z^2}{(R_1-\rho)^2+z^2}E(k^2)+K(k^2)\right] \tag{28}$$

and

$$A_\varphi(\rho,z)=\frac{I}{k}\sqrt{\frac{R_1}{\rho}}\left[\left(1-\frac{k^2}{2}\right)K(k^2)-E(k^2)\right], \tag{29}$$

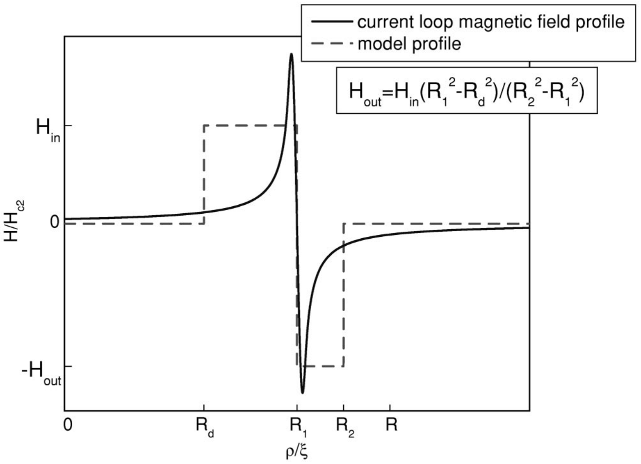

FIG. 20. The magnetic-field profile as produced by a current loop (solid curve) and its corresponding model profile (dashed curve).

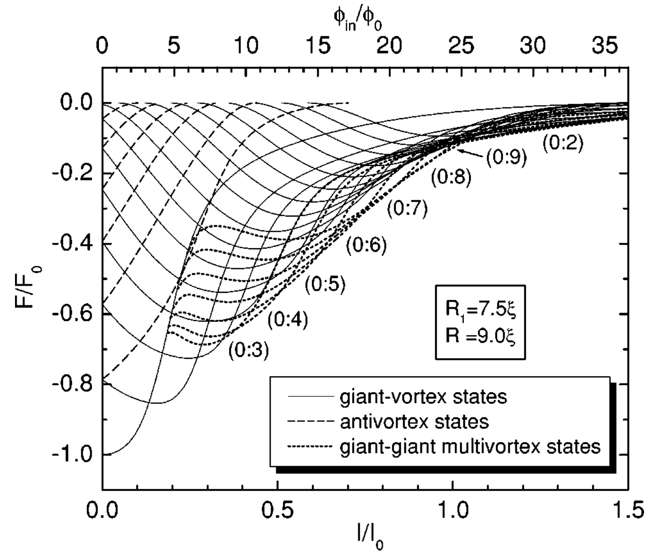

FIG. 21. The free energy of different vortex states as a function of the current in a loop with (a) $R_1/\xi = 7.5$, $R_2/\xi = R/\xi = 9.0$. Dashed curves depict the free energy of the antivortex states and dotted curves denote the giant-giant multivortex states.

with

$$k = 2\sqrt{\frac{R_1\rho}{(R_1+\rho)^2+z^2}}, \tag{30}$$

where $K(x)$ is the complete elliptic integral of the first kind and R_1 denotes the radius of the loop with current I.

The free energy is shown in Fig. 21 for a loop with radius $R_1 = 7.5\xi$, with a superconductor disk size $R = 9.0\xi$, as a function of current I measured in units of $I_0 = \pi\xi H_{c2}/\mu_0$. Typical values of I_0 are 3.29 mA for aluminum, to 0.823 A for high-temperature superconductors. One should compare these results with those presented in the H_{in}-R_d phase diagram (Fig. 17) and find that our previous model contains most of the essential physics of the system. The free-energy diagrams of both Figs. 14 and 21 show the reentrant behavior in total vorticity and the existence of the giant-giant multivortex configurations over a large region of the phase diagram.

VII. SUPERCONDUCTING DISK WITH A MAGNETIC DOT OR CURRENT LOOP ON TOP OF IT IN THE PRESENCE OF A BACKGROUND HOMOGENEOUS EXTERNAL MAGNETIC FIELD

In addition, we investigated the vortex structure of a superconducting disk in the presence of an inhomogeneous magnetic-field profile resulting from a ferromagnetic dot and a homogeneous external background magnetic field. In Figs. 22(a–c) we present the free energy as function of the external homogeneous field, for different magnetic dot thicknesses. The parameters were radius of the dot $R_1/\xi = 4.0$, radius of the superconducting disk $R/\xi = 6.0$ with thickness $d = 0.1\xi$, and the fixed magnetic-field profile of the ferromagnet, which is shown as an inset in Figs. 22(a–c). As expected, when a negative external field overwhelms the average of the positive magnetic field of the dot in the disk center, the antivortex states become energetically more favorable, and, conversely, when the positive external field becomes larger than the average negative value of the ferromagnetic dot field, we see that the ground state goes through successive giant-vortex states towards the normal state. For example, for a thickness of the magnetic dot $d_d = 0.1\xi$ we obtain an almost symmetrical figure with respect to $H_{ext} = -0.14H_{c2}$. However, with increasing magnetic dot thickness, the magnetic field of the ferromagnetic dot [given as an inset in Figs. 22(a–c)] becomes more pronounced and we obtain two sets of curves corresponding to the vortex and antivortex states, each of which has a minimum. These local minima occur at external field values which are approximately equal to the average field of the positive and negative region of the magnetic dot profile, respectively. The region between these two minima is characterized by a strong interplay of states.

For a current loop on top of the superconducting disk in a homogeneous external field we obtained qualitatively similar results. Also two sets of curves with two local minima are visible in the free energy for sufficiently large currents in the

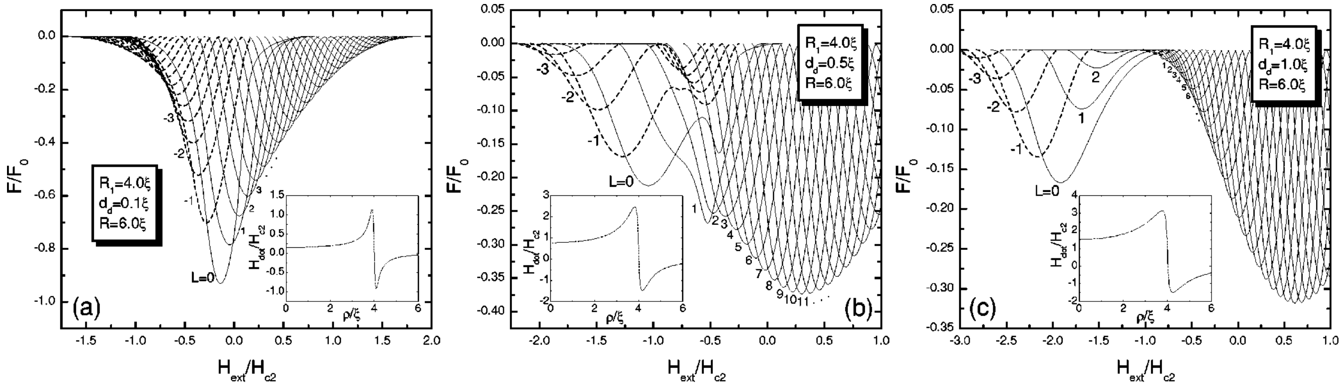

FIG. 22. The free energy of giant-vortex states as a function of the external magnetic field in a superconducting disk with a magnetic dot on top of it with parameters $R_1/\xi = 4.0$, $R/\xi = 6.0$ and (a) $d_d = 0.1\xi$, (b) $d_d = 0.5\xi$, and (c) $d_d = 1.0\xi$. Dashed curves depict the free energy of the antivortex states. Insets show the magnetic-field profile inside the superconducting disk created by the magnetic dot.

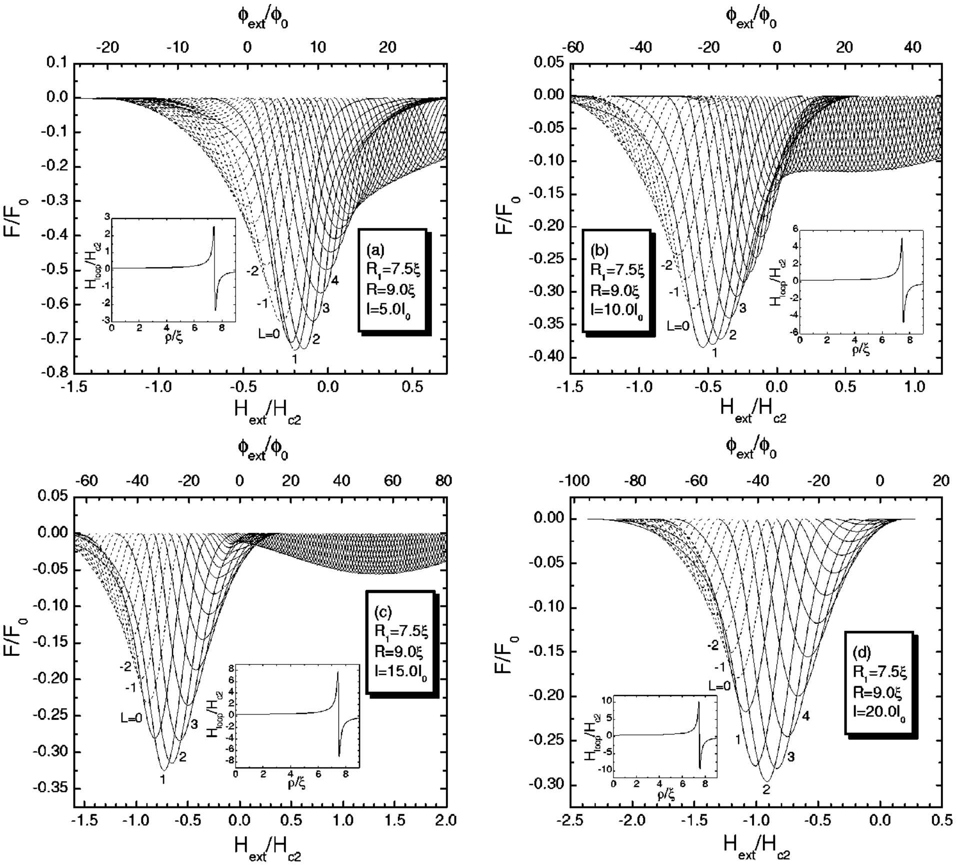

FIG. 23. The free energy of giant-vortex states as a function of the external magnetic field in a superconducting disk with a current loop on top of it with parameters $R_1/\xi=7.5$, $R/\xi=9.0$ and (a) $I/I_0=5.0$, (b) $I/I_0=10.0$, (c) $I/I_0=15.0$, and (d) $I/I_0=20.0$. Dashed curves depict the free energy of the antivortex states. Insets show the magnetic-field profile inside the superconducting disk created by the current loop.

loop [see Figs. 23(b,c)]. We show numerical results for a system consisting of a superconducting disk with $R/\xi=9.0$ and thickness $d=0.1\xi$, and a current loop with radius $R_1=7.5\xi$ (see Fig. 20). Just like in the previous case, minima in the free energy are related to average fields in the positive and negative region of the current loop magnetic-field profile. However, several differences exist. First, with increase of the thickness of the magnetic dot in the previous situation, the magnetic-field profile becomes more similar to our steplike field model. For the current loop case this is not so, and with increasing current in the loop the magnetic field becomes strongly inhomogeneous, rapidly increasing in the vicinity of the loop. As a consequence the minimum in the free energy for a negative external field is lower in energy, and, moreover, the other minimum slowly diminishes with further increase of the current in the loop. In this case even for negative applied external field, the positive peak in the magnetic field profile of the current loop is responsible for the stabilization of the positive L states, up to large $H_{ext}<0$ [see Fig. 23(d)]. It is obvious that the interplay between the external and the current loop magnetic field exhibits more interesting physics due to the strong field inhomogeneity.

VIII. CONCLUSION

We studied the superconducting state of a thin superconducting disk in the presence of an inhomogeneous magnetic field. A "model" steplike magnetic-field profile was considered, which is an approximation for the magnetic-field profile resulting from a magnetic disk or from a current loop. The superconducting disk is assumed sufficiently thin that the magnetic field produced by the superconducting currents can be neglected. The effects of the width of the positive field region, the position of the field, and the size of the superconducting disk on the vortex configuration were investigated. Numerous phase transitions were found, between states with different angular momentum number and between giant and multivortex states, plus transitions of the ground state between different multivortex configurations (giant-ring and giant-giant multivortex states). The model steplike magnetic field (total flux through the system equals zero) is found to stabilize the multivortex states both as the ground state (i.e., with minimal energy) and as metastable states. Increase of the width of the positive field region enhances the stability of the giant-giant multivortices, while enlarging the superconducting disk decreases the energy of the giant-ring multivortex state. In this case, the giant-giant multivortex states can also be the ground state but it represents a modified configuration—a giant vortex surrounded by antivortices, and the total vorticity equals the lowest vorticity of the giant-vortex states which are involved. We found that with an increase of the disk size, reentrant behavior of the total vorticity is possible. This behavior can also be seen by shifting the field profile towards the disk boundary, i.e., for the current loop magnetic field, when giant-giant multivortex configurations cover most of the superconducting phase diagram region. Comparison with results obtained for a real magnetic-field profile shows very good correspondence with our steplike models for the cases when most of the magnetic-flux is captured inside the superconducting disk. For a magnetic dot with a larger radius, the positive magnetic-field region of the inhomogeneous magnetic-field profile dominates and with increasing magnetic dot radius, the total flux in the superconductor also increases, which is different from our model where the total flux always equals zero. Thus, the positive part of the magnetic field profile determines mainly the superconducting states, which leads to slightly different physics—no reentrant behavior is present, more different superconducting states are possible, but without the giant-giant multivortex states with antivortices, since they are strongly correlated with a reentrance of the total vorticity.

Adding a homogeneous background magnetic field, besides the inhomogeneous field resulting from the magnetic dot, brings a qualitative difference in the free-energy diagram. When the external magnetic field is between the average field of the dot in the positive and the negative region, we observe a strong interplay of the different superconducting giant states. Moreover, with the increase of the thickness of the dot, we obtain two strong minima in the free energy, when the total field is approximately equal to zero in the $\rho < R_1$ and the $\rho > R_1$ region, respectively, where R_1 is the radius of the dot.

Here, we must emphasize that our results are only valid in the limit of very thin disks. It allowed us to separate the two GL equations and thus we neglected the magnetic field created by the superconducting currents.

ACKNOWLEDGMENTS

This work was supported by the Flemish Science Foundation (FWO-V1), the Belgian Inter-University Attraction Poles (IUAP-IV), the ‘‘Onderzoeksraad van de Universiteit Antwerpen’’ (GOA), and the ESF program on ‘‘Vortex matter.’’

APPENDIX: EIGENFUNCTIONS OF THE LINEARIZED FIRST GL EQUATION IN THE PRESENCE OF AN INHOMOGENEOUS MAGNETIC FIELD

1. Disk magnetic-field profile

The vector potential distribution is determined by the piecewise function [see Eq. (11) with $R_d = 0$]

$$A_0(\rho)=\begin{cases} H_{in}\rho/2, & 0\leqslant\rho\leqslant R_1 \\ -H_{out}\rho/2+H_{out}R_2^2/2\rho, & R_1\leqslant\rho\leqslant R_2 \\ 0, & R_2\leqslant\rho\leqslant R. \end{cases} \tag{A1}$$

The eigenfunctions of Eq. (15) are expressed in the following way:

$$f_{L,n}(\rho)=\begin{cases} f_{11}(\rho), & 0\leqslant\rho\leqslant R_1 \\ b_1 f_{21}(\rho)+b_2 f_{22}(\rho), & R_1\leqslant\rho\leqslant R_2 \\ d_1 f_{31}(\rho)+d_2 f_{32}(\rho), & R_2\leqslant\rho\leqslant R, \end{cases} \tag{A2}$$

where

$$f_{11}(\rho)=(H_{in}\rho^2/2)^{|L|/2}\exp(-H_{in}\rho^2/4)M(-\nu_{n,1}(\Lambda),|L|+1,H_{in}\rho^2/2),$$

$$f_{21}(\rho)=(H_{out}\rho^2/2)^{|L_2^*|/2}\exp(-H_{out}\rho^2/4)M(-\nu_{n,2}(\Lambda),|L_2^*|+1,H_{out}\rho^2/2),$$

$$f_{22}(\rho)=(H_{out}\rho^2/2)^{|L_2^*|/2}\exp(-H_{out}\rho^2/4)U(-\nu_{n,2}(\Lambda),|L_2^*|+1,H_{out}\rho^2/2),$$

$$f_{31}(\rho)=J_{|L|}(\sqrt{1+\Lambda}\rho),$$

$$f_{32}(\rho)=Y_{|L|}(\sqrt{1+\Lambda}\rho),$$

with $L_2^* = L - H_{out}R_2^2/2$, $\nu_{n,1}(\Lambda) = -(1+|L|-L)/2 + (1+\Lambda)/2H_{in}$, and $\nu_{n,2}(\Lambda) = -(1+|L_2^*|+L_2^*)/2 + (1+\Lambda)/2H_{out}$. Here $J_m(x)$ and $Y_m(x)$ are the Bessel functions of the first and second kind, $M(a,c,y)$ and $U(a,c,y)$ are the Kummer functions. To find the unknown constants $b_{1(2)}$, $d_{1(2)}$ and the eigenvalue Λ we have to join the different parts of $f_{L,n}(\rho)$ and their first derivatives at R_1 and R_2 as well as use the boundary condition $(\partial f/\partial\rho)|_{\rho=R}=0$. After a straightforward calculation we obtained

$$b_1=\frac{f_{111}f'_{221}-f_{221}f'_{111}}{f_{211}f'_{221}-f_{221}f'_{211}},\quad b_2=\frac{f_{211}f'_{111}-f_{111}f'_{211}}{f_{211}f'_{221}-f_{221}f'_{211}}, \tag{A3}$$

$$d_1=\frac{b_1(f_{212}f'_{322}-f_{322}f'_{212})+b_2(f_{222}f'_{322}-f_{322}f'_{222})}{f_{312}f'_{322}-f_{322}f'_{312}},$$

$$d_2=\frac{b_1(f_{312}f'_{212}-f_{212}f'_{312})+b_2(f_{312}f'_{222}-f_{222}f'_{312})}{f_{312}f'_{322}-f_{322}f'_{312}},$$

and the nonlinear equation for Λ,

$$\begin{aligned}&(f_{111}f'_{221}-f_{221}f'_{111})[f'_{31}(R)(f_{212}f'_{322}-f_{322}f'_{212})+f'_{32}(R)\\&\quad\times(f_{312}f'_{212}-f_{212}f'_{312})]+(f_{211}f'_{111}-f_{111}f'_{211})[f'_{31}(R)\\&\quad\times(f_{222}f'_{322}-f_{322}f'_{222})+f'_{32}(R)(f_{312}f'_{222}-f_{222}f'_{312})]\\&\quad=0,\end{aligned} \tag{A4}$$

where we introduced the following notations: $f_{ijk}=f_{ij}(R_k)$, $f'_{ijk}=(\partial f_{ij}/\partial\rho)|_{\rho=R_k}$. To obtain the correct Λ values we have to exclude from the spectrum of solutions of Eq. (A4), those which result in zeros of $f_{211}f'_{221}-f_{221}f'_{211}$ and $f_{312}f'_{322}-f_{322}f'_{312}$.

In the large radius limit $R\to\infty$, the result in the third region of the piecewise function can be replaced by asymptotics of the Bessel functions. Substituting them in Eq. (A4) we obtain

$$\Lambda=-1+\frac{1}{R^2}\left[\frac{\pi}{4}(3+2|L|)-\arctan\frac{d_1}{d_2}\right]^2. \tag{A5}$$

The value of $f_{L,n}(\rho)$ near the sample edge is equal to $\sqrt{d_1^2+d_2^2}$.

2. Ring magnetic-field profile

The vector potential distribution is given by Eq. (11) and, therefore, the eigenfunctions of Eq. (15) can be expressed as follows:

$$f_{L,n}(\rho)=\begin{cases} f_{11}(\rho), & 0\leqslant\rho\leqslant R_d \\ b_1 f_{21}(\rho)+b_2 f_{22}(\rho), & R_d\leqslant\rho\leqslant R_1 \\ d_1 f_{31}(\rho)+d_2 f_{32}(\rho), & R_1\leqslant\rho\leqslant R_2 \\ e_1 f_{41}(\rho)+e_2 f_{42}(\rho), & R_2\leqslant\rho\leqslant R, \end{cases} \tag{A6}$$

where

$$f_{11}(\rho)=f_{41}(\rho)=J_{|L|}(\sqrt{1+\Lambda}\rho),$$

$$f_{21}(\rho)=(H_{in}\rho^2/2)^{|L_2^*|/2}\exp(-H_{in}\rho^2/4)M(-\nu_{n,2}(\Lambda),|L_2^*|+1,H_{in}\rho^2/2),$$

$$f_{22}(\rho)=(H_{in}\rho^2/2)^{|L_2^*|/2}\exp(-H_{in}\rho^2/4)U(-\nu_{n,2}(\Lambda),|L_2^*|+1,H_{in}\rho^2/2),$$

$$f_{31}(\rho)=(H_{out}\rho^2/2)^{|L_3^*|/2}\exp(-H_{out}\rho^2/4)M(-\nu_{n,3}(\Lambda),|L_3^*|+1,H_{out}\rho^2/2),$$

$$f_{32}(\rho)=(H_{out}\rho^2/2)^{|L_3^*|/2}\exp(-H_{out}\rho^2/4)U(-\nu_{n,3}(\Lambda),|L_3^*|+1,H_{out}\rho^2/2),$$

$$f_{42}(\rho)=Y_{|L|}(\sqrt{1+\Lambda}\rho),$$

with $L_2^*=L+H_{in}R_d^2/2$, $L_3^*=L-H_{out}R_2^2/2$, $\nu_{n,2}(\Lambda)=-(1+|L_2^*|-L_2^*)/2+(1+\Lambda)/2H_{in}$, and $\nu_{n,3}(\Lambda)=-(1+|L_3^*|+L_3^*)/2+(1+\Lambda)/2H_{out}$. The constants $b_{1(2)}$, $d_{1(2)}$, and $e_{1(2)}$ are given by the following expressions:

$$b_1=\frac{f_{11d}f'_{22d}-f_{22d}f'_{11d}}{f_{21d}f'_{22d}-f_{22d}f'_{21d}},\quad b_2=\frac{f_{21d}f'_{11d}-f_{11d}f'_{21d}}{f_{21d}f'_{22d}-f_{22d}f'_{21d}}, \tag{A7}$$

$$d_1=\frac{b_1(f_{211}f'_{321}-f_{321}f'_{211})+b_2(f_{221}f'_{321}-f_{321}f'_{221})}{f_{311}f'_{321}-f_{321}f'_{311}},$$

$$d_2=\frac{b_1(f_{311}f'_{211}-f_{211}f'_{311})+b_2(f_{311}f'_{221}-f_{221}f'_{311})}{f_{311}f'_{321}-f_{321}f'_{311}},$$

$$e_1=\frac{d_1(f_{312}f'_{422}-f_{422}f'_{312})+d_2(f_{322}f'_{422}-f_{422}f'_{322})}{f_{412}f'_{422}-f_{422}f'_{412}},$$

$$e_2=\frac{d_1(f_{412}f'_{312}-f_{312}f'_{412})+d_2(f_{412}f'_{322}-f_{322}f'_{412})}{f_{412}f'_{422}-f_{422}f'_{412}},$$

and the spectrum of Λ values is determined by the nonlinear equation

$$\begin{aligned}&[(f_{11d}f'_{22d}-f_{22d}f'_{11d})(f_{211}f'_{321}-f_{321}f'_{211})+(f_{21d}f'_{11d}\\&\quad-f_{11d}f'_{21d})(f_{221}f'_{321}-f_{321}f'_{221})][f'_{41}(R)(f_{312}f'_{422}\\&\quad-f_{422}f'_{312})+f'_{42}(R)(f_{412}f'_{312}-f_{312}f'_{412})]+[(f_{11d}f'_{22d}\\&\quad-f_{22d}f'_{11d})(f_{311}f'_{211}-f_{211}f'_{311})+(f_{21d}f'_{11d}-f_{11d}f'_{21d})\\&\quad\times(f_{311}f'_{221}-f_{221}f'_{311})][f'_{41}(R)(f_{322}f'_{422}-f_{422}f'_{322})\\&\quad+f'_{42}(R)(f_{412}f'_{322}-f_{322}f'_{412})]=0\end{aligned} \tag{A8}$$

[like in the previous case, we have to exclude from the solutions of Eq. (A8), those which result in zeros of $f_{21d}f'_{22d}-f_{22d}f'_{21d}$, $f_{311}f'_{321}-f_{321}f'_{311}$ and $f_{412}f'_{422}-f_{422}f'_{412}$].

In the large radius limit $R\rightarrow\infty$, the $f_{L,n}(\rho)$ value near the sample edge is approximately equal to $\sqrt{e_1^2+e_2^2}$, and Λ is given by Eq. (A5) with $d_{1(2)}$ replaced by $e_{1(2)}$.

---

*Permanent address: Donetsk Physical & Technical Institute, National Academy of Sciences of Ukraine, Donetsk 83114, Ukraine.

†Electronic address: peeters@uia.ua.ac.be

[1] O. Buisson, P. Gandit, R. Rammel, Y. Y. Wang, and B. Pannetier, Phys. Lett. A **150**, 36 (1990).

[2] L. F. Chibotaru, A. Ceulemans, V. Bruyndoncx, and V. V. Moshchalkov, Nature (London) **408**, 833 (2000).

[3] A. K. Geim, I. V. Grigorieva, S. V. Dubonos, J. G. S. Lok, J. C. Maan, A. E. Filippov, and F. M. Peeters, Nature (London) **390**, 259 (1997).

[4] P. S. Deo, V. A. Schweigert, F. M. Peeters, and A. K. Geim, Phys. Rev. Lett. **79**, 4653 (1997).

[5] R. Benoist and W. Zwerger, Z. Phys. B: Condens. Matter **103**, 377 (1997).

[6] V. A. Schweigert and F. M. Peeters, Phys. Rev. B **57**, 13 817 (1998).

[7] V. A. Schweigert, F. M. Peeters, and P. S. Deo, Phys. Rev. Lett. **81**, 2783 (1998).

[8] J. J. Palacios, Physica B **256-258**, 610 (1998).

[9] J. J. Palacios, Phys. Rev. B **58**, R5948 (1998).

[10] E. Akkermans and K. Mallick, J. Phys. A **32**, 7133 (1999).

[11] P. S. Deo, F. M. Peeters, and V. A. Schweigert, Superlattices Microstruct. **25**, 1195 (1999).

[12] G. M. Braverman, S. A. Gredeskul, and Y. Avishai, Phys. Rev. B **59**, 12 039 (1999).

[13] B. J. Baelus, F. M. Peeters, and V. A. Schweigert, Phys. Rev. B **63**, 144517 (2001).

[14] M. J. Van Bael, L. Van Look, K. Temst, M. Lange, J. Bekaert, G. Guentherodt, V. V. Moshchalkov, and Y. Bruynseraede, Physica C **332**, 12 (2000).

[15] M. Lange, M. J. Van Bael, L. Van Look, K. Temst, J. Swerts, G. Guentherodt, V. V. Moshchalkov, and Y. Bruynseraede, Europhys. Lett. **53**, 646 (2001).

[16] J. I. Martin, M. Velez, A. Hoffmann, Ivan K. Schuller, and J. L. Vicent, Phys. Rev. B **62**, 9110 (2000).

[17] I. K. Marmorkos, A. Matulis, and F. M. Peeters, Phys. Rev. B **53**, 2677 (1996).

[18] Sa-Lin Cheng and H. A. Fertig, Phys. Rev. B **60**, 13 107 (1999).

[19] R. Sasik and T. Hwa, cond-mat/0003462 (unpublished).

[20] S. V. Yampolskii and F. M. Peeters, Phys. Rev. B **62**, 9663 (2000).

[21] J. Govaerts, G. Stenuit, D. Bertrand, and O. van der Aa, Phys. Lett. A **267**, 56 (2000).

[22] B. J. Baelus, F. M. Peeters, and V. A. Schweigert, Phys. Rev. B **61**, 9734 (2000).

[23] V. A. Schweigert and F. M. Peeters, Phys. Rev. Lett. **83**, 2409 (1999).

[24] J. J. Palacios, Phys. Rev. Lett. **84**, 1796 (2000).

[25] V. A. Schweigert and F. M. Peeters, Physica C **332**, 266 (2000).